Supplementary materials — From real-time to long-term source apportionment of PM₁₀ using high-time-resolution measurements of aerosol physical properties: Methodology and example application at an urban background site (Aosta, Italy)

Henri Diémoz et al.

6 S1 Map of Aosta

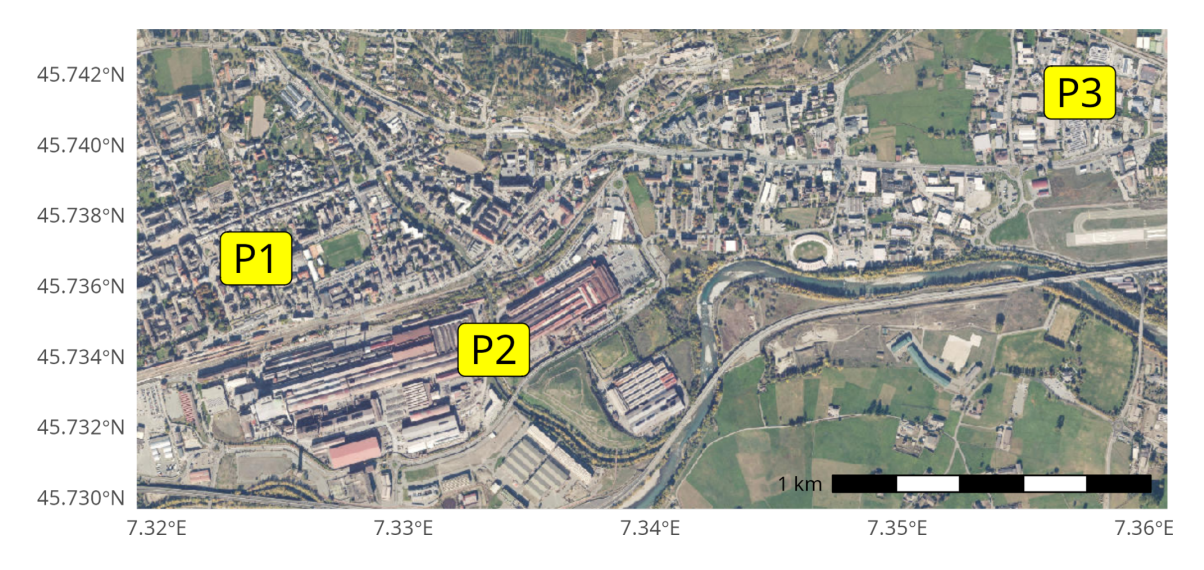


Figure S1: Aerial photograph of Aosta city taken in 2021 (Regione Valle d'Aosta, 2021), with labels indicating key locations: the Aosta-downtown air quality station (P1), the steel mill (P2), and the Aosta-Saint-Christophe solar-atmospheric observatory (P3).

S2 Supplementary details on Palas Fidas 200

The Palas Fidas 200, currently housed in a temperature-stabilised air quality cabin at the Aosta–Downtown station, was originally acquired as the 200S variant, which features a stainless-steel weather-proof casing for outdoor operation. Ambient air is sampled at a rate of $4.8\,\mathrm{L\,min^{-1}}$ into the instrument, with condensation effects mitigated by the integrated 'Intelligent Aerosol Drying System' (IADS). This module dynamically adjusts the sample temperature based on ambient conditions (measured by an integrated weather station), at a minimum temperature of $23^{\circ}\mathrm{C}$. The maximum heating output is 90 W. Without temperature regulation, water condensating on particles in high humidity conditions could cause distorting size measurements. Additionally, according to the manual (PALAS GmbH, 2016), residual water content is detected, and the mass of liquid droplets is subtracted to improve accuracy.

Particle detection is based on white light scattering at a 90° angle (Pletscher et al., 2016). Border zone errors are removed using a specialized T-aperture optical design, and coincidence events are corrected through digital particle analysis. The instrument processes particle size distributions and retrieves PM concentrations using its built-in proprietary algorithm, PM_ENVIRO_0011. For completeness, the operational steps of this algorithm, only briefly outlined in the manual (PALAS GmbH, 2016), are reported below:

1. The initial particle size distribution, referred to a latex-equivalent diameter, is adjusted to a distribution with a representative refractive index for the environment. It is presumable that this step is introduced to mitigate the sensitivity of OPCs measurements to refractive index (Ferrero et al., 2011; Chien et al., 2016), though some studies suggest these errors are minimal in urban settings (Hasheminassab et al., 2014; Sowlat et al., 2016).

23

24

25

26

27

28

29

30

31

32

33

34

35

36

37

38

39

40

41

43

44

46

47

48

49

50

51

52

53

54

55

56

57

58

59

60

61

62

63

64

66

67

- 2. Optical diameters are converted to aerodynamic diameters (the manual provides no further details on the method used).
- 3. The shape of the particle size distribution is analysed, and density parameters are derived.
- 4. Particle mass concentration is estimated using these size-dependent conversion functions.

Verification of equivalence (e.g., Marsteen and Hak, 2021) has been routinely performed at the Aosta-Downtown against the gravimetric method. The Palas Fidas 200 consistently demonstrated relative observation uncertainties within 25 % at the PM₁₀ EU daily limit value, in agreement with Directive 2008/50/EC (European Commission, 2008). Hence, no corrections to the Fidas PM₁₀ concentrations were deemed necessary. Monthly maintenance includes the following procedures: automatic offset adjustment, leakage testing, sampling head cleaning, pump filter replacement, sampling flow rate measurement, photomultiplier tube (PMT) testing using monodust aerosols, and pump suction output verification with replacement if efficiency drops below 80 %.

We set the sampling resolution of the Fidas to 1 min instead of the default 1 s. This adjustment is particularly important because we found that coarse (and sparser) particles are not adequately sampled at higher frequencies. Particle size distribution and PM concentration datasets are automatically extracted from the instrument via the Fidas MODBUS interface, eliminating the need for manual operation of the 'PDAnalyze' program.

S3Choice of aethalometer wavelengths to calculate the Delta-C quan-45 tity

Various wavelength combinations can be employed to calculate Delta-C, for example 370 nm or 470 nm can be chosen as the lower limit, and 880 nm or 950 nm as the upper limit.

For our dataset, the choice of the upper limit is unimportant, as also found by Zotter et al. (2017), since the correlation index between the combinations using 880 nm and 950 nm is nearly 1 (0.99988). Hence, we use 880 nm, the conventional wavelength for defining eBC. As for the lower limit, our choice is based on two factors. First, previous investigations in Aosta and its outskirts (Diémoz et al., 2020) found that the correlation index between levoglucosan concentrations, an unambiguous marker of fresh biomass burning, and aethalometer measurements at 370 nm is very high (ranging from 0.82 to 0.92, depending on the site). Second, we analysed the patterns of the difference between aethalometer mass concentrations at 370 nm and 880 nm, as well as between 470 nm and 880 nm, at different temporal scales (Fig. S2). The results indicate that the former quantity exhibits greater variability between night and day, and between winter and summer, suggesting that it may more closely track the variations in the biomass burning contribution to PM than the latter quantity.

It should be noted that the influence of volatile or secondary biogenic organic compounds at 370 nm (Vecchi et al., 2014; Romonosky et al., 2016; Xie et al., 2019) is sometimes considered an interfering factor in determining the biomass burning contribution (Zotter et al., 2017). However, if such interference were significant at our site, the source apportionment algorithm should have identified it as a separate factor. Nonetheless, the strong agreement between the biomass burning contribution derived from RASPBERRY and that obtained from the chemical PMF (correlation index $\rho = 0.95$, Fig. 8 in the main text) retrospectively validates this specific choice of wavelengths. Therefore, in this study, we retain the original definition of Delta-C by Allen et al. (2011) and Wang et al. (2011) using the two-wavelength aethalometer, i.e.:

(S1)
$$Delta-C = NeBC(370 \text{ nm}) - NeBC(880 \text{ nm})$$

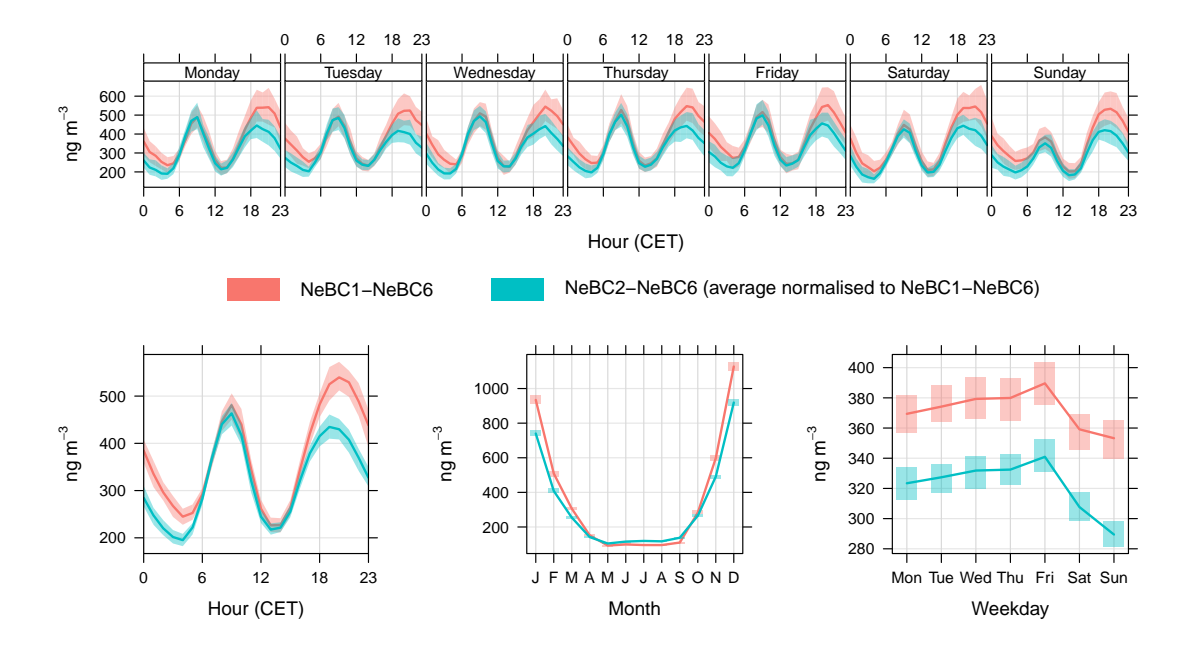


Figure S2: Average time patterns of the difference between NeBC $_{370~\rm nm}$ (NeBC1) and NeBC $_{880~\rm nm}$ (NeBC6), as well as between NeBC $_{470~\rm nm}$ (NeBC2) and NeBC $_{880~\rm nm}$, at different temporal scales. For ease of visualisation, the latter quantity has been normalised, on average, to the former.

S4 Supplementary details on Aerosol Magee Scientific AE33 aethalometer

69

70

71

72

73

74

75

76

77

78

79

80

81

82

83

84

85

86

87

88

89

90

91

92

93

94

95

Two primary instrumental artefacts influence the accuracy of aethalometer measurements and require correction: the filter-loading effect and the multiple-scattering enhancement effect (Weingartner et al., 2003). The AE33 dual-spot technology compensates for the filter-loading effect in real time, while the multiple-scattering enhancement is addressed using a scattering correction coefficient (C). In this study, we employ the default instrument manufacturer fixed parameters ($C_0 = 1.39$ for filter tape M8060; nominal MAC value of 7.77 m² g⁻¹ at 880 nm) and, accordingly, we adopt the term NeBC ('nominal' eBC, Savadkoohi et al., 2024) to denote the AE33 output obtained under nominal settings. Although recent research demonstrates that using instrument- and site-specific parameters (Grange et al., 2020; Ferrero et al., 2024), or harmonised coefficients (Zanatta et al., 2016; Savadkoohi et al., 2024), leads to more accurate determination of the absorption coefficients, our approach is guided by two criteria: (i) ensuring the algorithm is simple and straightforward to implement, and (ii) assuming that temporal and spectral variations in aerosol light absorption are more important in PMF analysis than the absolute accuracy of b_{abs} values. Moreover, determining site-specific parameters such as the MAC requires data from ancillary sources, which might not be available at all locations. While these refinements are essential for analysing long-term trends (Grange et al., 2020; Savadkoohi et al., 2024), they are left for future research. However, we note that the correlation, in Aosta-Downtown, between EC from chemical analyses and NeBC at both 880 and 950 nm is already very strong (Pearson's $\rho = 0.93$).

The following data quality controls are applied on the aethalometer measurements:

- Occasional negative values at the 1-minute scale are retained to avoid biases in average calculations.
 However, negative NeBC values in 1-hour averages are excluded.
- Measurements yielding negative Delta-C at the 1-hour scale are also removed.
- Extremely high NeBC concentrations (>15000 ng m⁻³) are discarded, as these outliers are often associated with circumstantial events or measurement anomalies unsuitable for algorithm training.
- Quality control thresholds proposed by Aujay-Plouzeau (2020), including AAE and the R² of spectral fits at the 15-minute scale, were tested but not adopted since, in our case, they were not

always representative of measurement quality.

96

97

98

99

100

101

102

103

104

105

106

107

108

109

110

111

113

114

115

116

117

118

119

120

121

122

123

124

125

126

127

128

129

130

- The final dataset was visually inspected to remove any remaining anomalous data.

Regular maintenance is performed monthly and includes: clean air test; inspection and cleaning of the optical chamber, insect trap, and sampling line; lubrication of the optical chamber cursors; ND filter test; bypass cartridge replacement if necessary; stability test.

An important aspect of our AE33 setup relates to its sampling line. During a 2019 experimental campaign with a mobile laboratory (Diémoz et al., 2020), the AE33 was operated without a sampling head for technical reasons. This configuration was inadvertently replicated in the permanent installation at the Aosta–Downtown station, resulting in BC measurements in total suspended particles (TSP). This oversight was identified recently and an update to the setup with a PM_{10} cyclone and a drier is scheduled. Future studies will assess the impact of this change, however it is uncertain whether the absence of a PM_{10} inlet has significantly influenced measurements. Indeed, the majority of light-absorbing particles reside in the fine fraction. Some high-frequency noise is observed in 1-minute NeBC data at very low concentrations, such as during summer, potentially amplified by the lack of a drier. To mitigate these effects, aethalometer measurements were averaged to 1-hour intervals, and data from all instruments in Aosta–Downtown were harmonised to this temporal resolution.

112 S5 Chemical PMF configuration

As outlined in Sect. 2.4 of the main text, two separate chemical PMF analyses are performed due to the alternating sampling schedule and differing chemical characterisations. No missing values are included in both PMF input datasets, and new year's days are excluded from the analysis each year. Dataset 1 (water-soluble ions alongside EC/OC and levoglucosan) consists of 383 samples and 12 variables. Ca²⁺ and Mg²⁺ are set as weak, given their high proportion of values at or near detection limits, 23 % and 21 % respectively. This choice may slightly affect the PMF output, particularly the separation of traffic-related and coarse particle resuspension contributions. NH4⁺ is also classified as weak as recent findings suggest that ammonium volatilisation likely occurred post-sampling due to operational practices with the sequential sampler and filter storage. Updated procedures have since been introduced to address these issues. PM₁₀ is set as the total variable, while the remaining eight variables are classified as strong. Dataset 2 (water-soluble ions and metals) includes 699 samples and 18 species. The following species are treated as weak: Al, as it tends to form an isolated factor, a fact that is only partially correlated with long-range transport of desert dust (contamination of samples or local sources other than desert dust are possible reasons); Zn, due to a spurious concentration increase over time likely caused by analytical issues; Co, since many measurements are close to detection limits, which varies over time with changes in analytical techniques; NH₄⁺, Ca²⁺, and Mg²⁺, for the same reasons outlined for the first dataset. Additionally, days with single outlier values for Cd, Cu, Zn, Co, Pb, and Mg are excluded from the analysis.

¹³¹ S6 Physical PMF uncertainty configuration

The uncertainty framework employed in this study follows the methodology outlined by Vörösmarty et al. (2024). The free parameters A, α , and C_3 are configured as shown in Table S1.

Table S1: Parameters for the calculation of the overall uncertainty following the same framework as in Vörösmarty et al. (2024). The total variable PM_{10} and the size channels at $d > 6 \,\mu$ m are set as weak variables in PMF; the corresponding values in this table have already been mutiplied by 3.

	PM_{10}	Delta-C	$\mathrm{NeBC}(470950\mathrm{nm})$	$d<2\mu m$	$2\mu\mathrm{m} < d < 6\mu\mathrm{m}$	$d > 6 \mu m$
A	3	1	1	1	1	1
α	0.01	0.01	0.01	0.01	0.01	0.01
C_3	0.35	0.05	0.05	0.10	0.35	0.45

The three parameters are finely tuned based on the following considerations: (i) initial values are taken from the scientific literature (e.g., Zhou et al., 2005a; Ogulei et al., 2006, 2007; Gu et al., 2011; Vörösmarty et al., 2024), with particular attention on increasing uncertainty for larger particle sizes; (ii) the distribution of residuals after factorisation is examined, and uncertainties are adjusted to ensure that scaled residuals generally fall within ± 3 (Norris et al., 2014), and that the $\frac{Q_{true}}{Q_{exp}}$ ratio for each species remains close to 1; (iii) profiles are verified to ensure they are physically meaningful, with contributions that are as uncorrelated as possible to each other. Additionally, as noted by Paatero (2018), when mixing different physical quantities in a single PMF, their residuals must be appropriately weighted in Q. This ensures that the influence of each quantity on the final solution (i.e., the total contribution of their scaled residuals in Q) is well balanced. Achieving an optimal solution required several tests, as small variations in the uncertainty configuration often produced unpredictable changes in the final outcome. For instance: if the uncertainty of the largest size bins is too high, contributions from desert dust and local resuspension tend to mix; if the uncertainty of the NeBC concentrations is too high, the size-related portion of the PMF dominates due to the larger number of size classes, leading to additional size modes that lack clear physical interpretation; for some combinations, the contributions of traffic emissions and residential biomass burning are rendered unrealistically small. Interestingly, similar issues with the mass of the traffic factor were reported by Forello et al. (2023). Importantly, during this process, we avoided 'tuning' the results of physical PMF to match those of chemical PMF, ensuring the independence of the two datasets. Nevertheless, prior knowledge or estimates from supplementary measurements or analyses can be used to inform the uncertainty assessment at the discretion of the user.

It may be noticed that the uncertainty for the largest size channels ($d > 6 \,\mu m$) is rather high. This reflects the relatively low number of large particles and their 'shot' nature, which introduces greater uncertainty when considered in a Poisson-based perspective. Indeed, these bins feature a few peak values emerging from a background of zeros, whose frequency can reach up to 30 %. Hence, these size channels, along with the total variable PM_{10} , are classified as weak variables in the PMF configuration to prevent them to be displaced in subsequent tests (the corresponding uncertainties reported in Table S1 have already been multiplied by 3).

During testing, as suggested by previous studies (e.g., Zhou et al., 2004; Thimmaiah et al., 2009; Zhou et al., 2005b), an alternative approach was evaluated in which the largest size bins were grouped (in sets of three to five, depending on the size) to mitigate issues associated with low particle counts and to improve the signal-to-noise ratio (SNR). Although bin grouping effectively enhanced the SNR, it hindered the separation of the two coarse factors (desert dust and local resuspension), hence we decided not to implement this methodology.

Regarding the absorption component (NeBC), it might be argued that the associated uncertainties are lower than those reported in other studies (e.g., Forello et al., 2019; Rigler et al., 2020). In particular, Forello et al. (2023) applied an uncertainty as high as 50 % for b_{abs} to prevent convergence issues when coupling absorption data with chemical data in the PMF. With such high uncertainty, combined with the smaller number of optical variables compared to chemical species, it is evident that the optical information did not guide the PMF in their study, but rather followed the factorisation. In contrast, our approach aims to ensure that both the optical and physical parts contribute to determining the final solution. Consequently, the uncertainty values we use should not be interpreted as true measurement uncertainties but rather as an adjustment to balance the influence of different input variables on the Q metric.

S7 Selection criteria for optimal number of factors in the chemical PMFs and associated quality metrics

Factorisations with up to seven factors were explored for both chemical PMFs, based on water-soluble ions combined with EC/OC and levoglucosan (dataset 1), or ions and metals (dataset 2). In both cases, six-factor solutions were selected as optimal.

For chemical dataset 1, the 5-factor PMF solution results in traffic emissions and crustal sources merging, likely due to their interaction through dust resuspension. Conversely, the 7-factor solution increases the $\frac{Q_{true}}{Q_{exp}}$ ratio and leads to NH4⁺ separating into its own factor, with no physical reasons. The selected 6-factor solution (Fig. S3) is achieved with 100 runs, yielding $Q_{rob} = 1065$ (same value for Q_{true}) and a $\frac{Q_{true}}{Q_{exp}}$ ratio of 1.5. The PM₁₀ is reconstructed with an R² of 0.8, an intercept of 4.0 µg m⁻³ and a slope of 0.7. All strong species are reproduced with $R^2 > 0.9$. To better distinguish the biomass burning factor, three constraints are applied: levoglucosan is maximally pulled up in the biomass burning factor and set to zero in the traffic and sodium chloride (road salting) factors, resulting in a dQ increase of just 0.37 %. The constrained DISP test reveals no swaps or decreases in Q. The BS test is conducted with 100 bootstraps, a minimum correlation R-value of 0.6, and a block size of 30. Corrections to the erroneous block size value suggested by EPA PMF5 are applied based on Patton et al. (2009) and Bhandari et al. (2022), with the final value determined using the 'b.star' routine from the 'np' R package (Hayfield and Racine, 2008). All boot factors match their respective base case factors 100 %, except for the traffic factor (91 % match, with 9 % attributed to the crustal factor) and the crustal factor (97 % match, with 3 % attributed to the sulfate-rich factor). These slight mismatches can be physically justified by the fact that traffic and crustal sources are linked through resuspension, while sulfates are often associated with the crustal component during summer. BS-DISP is performed as well, by actively displacing the most representative species among the strong ones (EC, NO₃, SO₄²⁻, Cl, and levoglucosan). The test shows no significant decrease in Q (< 0.5 %), however, swaps are already observed at $dQ^{max} = 0.5$ between the road salting and biomass burning factors. This is likely due to their concurrently high values during winter and the limited number of measured species analysed, indicating that dataset 1 is affected to some extent by rotational ambiguity.

For chemical dataset 2, the 5-factor solution results in nitrate and part of sulfate merging into a single factor, while some sulfate and crustal elements combine into another. Using 7 factors, the Q value remains comparable to that of the 6-factor solution, however Cd is unphysically separated into its own factor. The 6-factor solution (Fig. S4) is therefore selected, yielding $Q_{rob} = 9704$, $Q_{true} = 9725$ and $\frac{Q_{true}}{Q_{exp}} = 2.3$. The BS test is conducted using 100 bootstraps with a minimum correlation R-value of 0.6 and a block size of 39. All factors are correctly mapped in over 98 % of cases, with only minor swaps observed between the sulfate- and nitrate-rich factors. The DISP test reveals no swaps or decreases in Q. BS-DISP is performed by actively displacing the following strong and representative species: Fe, Ni, Cu, Cl⁻, NO $_3^-$, SO $_4^{2-}$. No swaps and no significant decreases are observed in Q (dQ < 0.2 %). The measured PM₁₀ is reconstructed by the PMF with an R^2 of 0.9, an intercept of 1.4 µg m⁻³ and a slope of 0.88. Most strong species are reproduced with $R^2 \ge 0.9$.

It should be noted that for both datasets, additional constraints could be applied to pull down or set to zero Ca²⁺ and Mg²⁺ concentrations, clear markers of resuspended dust, in the 'traffic emissions' profile. This adjustment would redefine the 'traffic' profile as 'fossil fuel' or 'traffic exhaust', i.e. without any non-exhaust component. The choice is subjective, with both advantages and disadvantages depending on the approach. Considering that Palas Fidas 200 is only sensitive to particles with diameters >0.18 µm, and that the contribution of traffic in a broader sense (exhaust and non-exhaust) may be more relevant in a policy perspective, we choose not to introduce additional constraints on Ca²⁺ and Mg²⁺, and keep the partial correlation between crustal matter and traffic emissions as it emerges from the PMF. For consistency, a similar logic is used in the physical PMF.

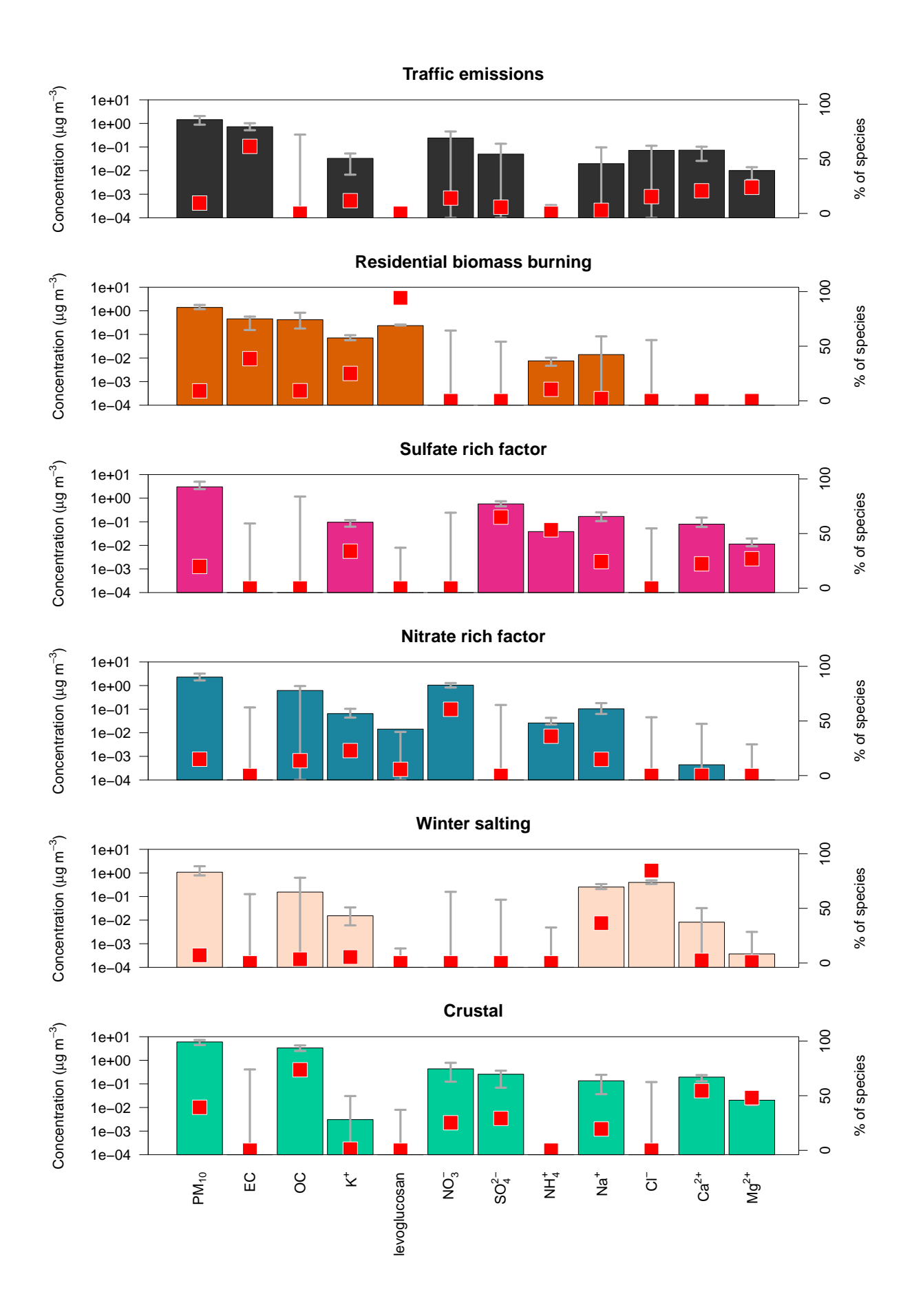


Figure S3: PMF solution profiles obtained with dataset 1 (anion/cation, EC/OC and levoglucosan). Bars represent the absolute mass contribution of each species in each factor (left y-axis), while the small squares represent the percentage contribution of each factor to each species (right y-axis). The error bars depict the $dQ^{max} = 4$ range of the DISP test.

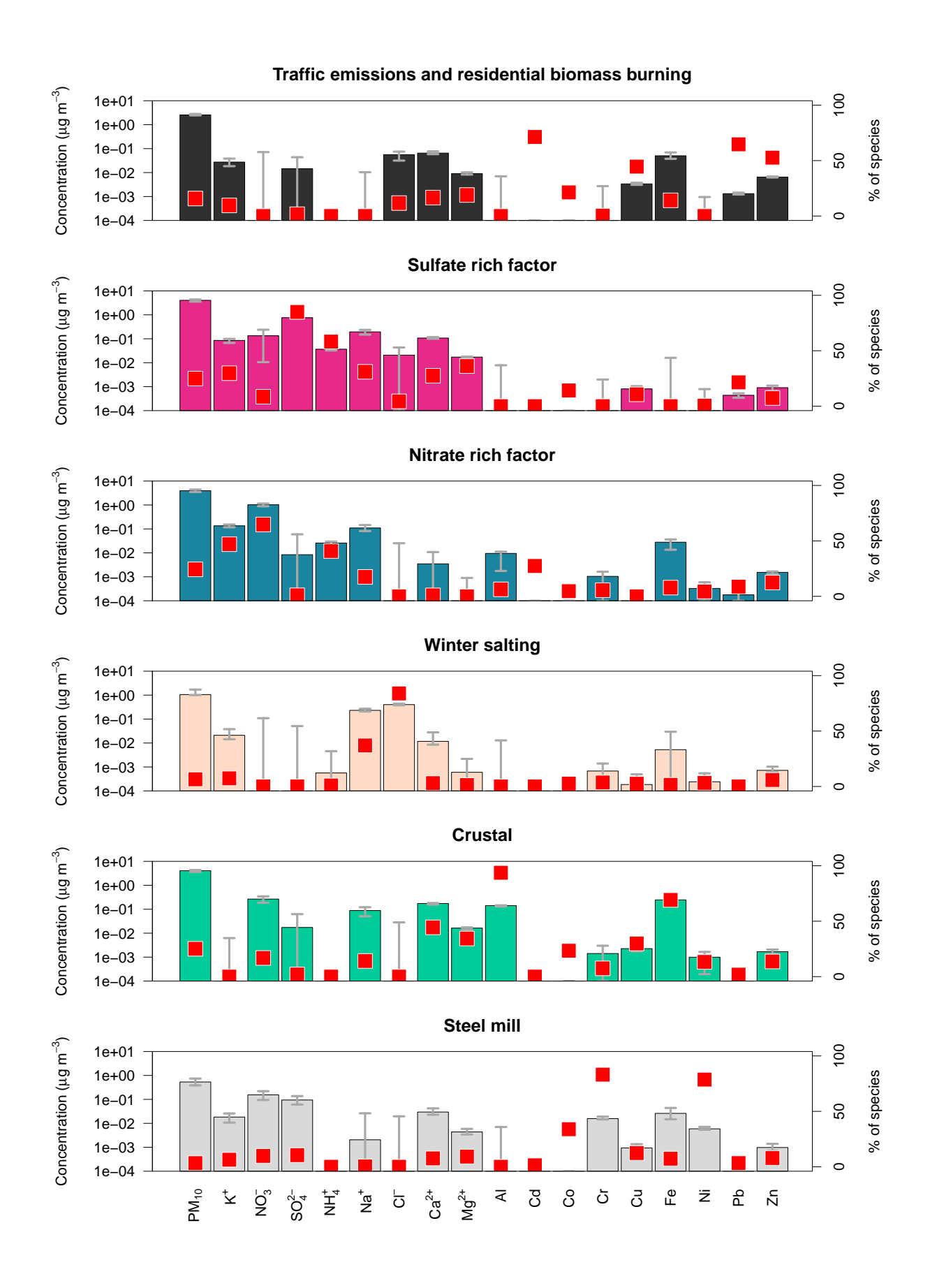


Figure S4: PMF solution profiles obtained with dataset 2 (anion/cation and metals).

S8 Selection and fine-tuning of the optimal physical PMF solution

225

245 246

247

248 249

250

251

252

253

255

256

257

258

259

260

261

262

263

264

265

266

267

268

269

4000 samples, each containing 70 species and the total variable PM_{10} , were given as input to the PMF. 226 55 species were classified as strong variables: Delta-C, NeBC(470-950 nm) and volume size distributions at diameters <6 µm, as described in Sect. S6. No missing values were present in the input dataset. The 228 remaining size bins were set as weak. Solutions were explored with a variable number of factors up to 7, 229 with the 6-factor solution being considered the best. This choice was based on the following criteria: (i) 230 the physical interpretability of the profiles; (ii) the $\frac{Q_{true}}{Q_{exp}}$ ratio; (iii) the shape and the range of the scaled 231 residual distribution. The 5-factor solution showed a higher $Q \sim 2$, with $\frac{Q_{true}}{Q_{exp}}$ for Delta-C reaching 25, due to the merging of traffic emissions and residential biomass burning factors. The 7-factor solution 232 233 yielded an overall $\frac{Q_{true}}{Q_{exp}}$ ratio of 1.2, and an additional factor with a modal diameter of approximately 234 1 μm. Interestingly, a similar intermediate mode has been observed in previous studies (e.g., Bernardoni 235 et al., 2017), and has been linked to various sources, including coal combustion (Pakkanen et al., 2001; 236 Salma et al., 2005), traffic-related emissions as a secondary maximum (Gu et al., 2011), resuspension 237 (Sowlat et al., 2016), and primary emissions from heavy-duty vehicles (Rivas et al., 2020), or even to 238 inconsistencies between optical and aerodynamic diameter determinations (Vu et al., 2015). In our 239 study, for the 7-factor solution, this factor shows strong correlations with many others, complicating 240 its physical interpretation. Even more importantly, its inclusion leads to a significant reduction in 241 the biomass burning contribution, despite the profile of the intermediate factor showing zero NeBC 242 concentration or Delta-C. Consequently, the 7-factor solution was discarded in favour of the more interpretable 6-factor solution.

To fine-tune the 6-factor solution, 9 samples were excluded due to their $\frac{Q_{true}}{Q_{exp}}$ ratio being ≥ 5 . Curiously, these samples were not related to events characterised by high PM₁₀ concentrations, but rather by quite low concentrations, as also found by Bhandari et al. (2022). This suggests that removing these low values likely enabled the PMF to find a better rotation. The resulting overall $\frac{Q_{true}}{Q_{exp}}$ ratio is 1.4 ($Q_{exp} = 195670$) and single species $\frac{Q}{Q_{exp}}$ generally within 1–2 except the largest size bins with values slightly > 2 (the uncertainty was not further tuned for those classes in order not to complicate the configuration). Q_{true} and Q_{rob} differ by only 0.8 %, meaning that outliers have almost no effect. After the base run, two constraints are applied: the NeBC at 880 nm is pulled down in the local coarse dust resuspension and in the secondary condensation mode factors, to enhance separation from the combustion-related factors (i.e., traffic emissions and residential biomass burning). This refinement of the optical absorption properties, also employed in other works (Savadkoohi et al., 2025), is based on the negligible EC concentrations in the crustal and sulfate-rich modes in the chemical PMF and transfers some mass, likely due to resuspension, from the local coarse factor to the traffic emission one. The constraint at 880 nm is sufficient to reduce NeBC levels at the other aethalometer wavelengths. Both constraints increase Q by only 0.25 %. The bootstrap (BS), displacement (DISP) and BS-DISP tests were performed. The BS test has been applied with 100 runs, minimum correlation value 0.6 and block size 130. In the BS-DISP tests, only a few representative species were set as actively displaced due to the already high number of samples, i.e. Delta-C, NeBC(880 nm), and VSDs at diameters of about 200 nm, 500 nm, 2 μm and 6 μm (this latter is the largest size bin set as strong variable). Zero swaps were detected in all tests, the boot factors were assigned in 100 % of the cases to their respective base factors, and no decreases in Q were found in the DISP and BS-DISP tests. This shows that the physical PMF is rotationally very stable. The total variable, PM_{10} , is reconstructed with $R^2 = 0.97$, intercept $-0.99 \,\mathrm{ug}\,\mathrm{m}^{-3}$ and slope 1.07. After the CMB-like extrapolation of the whole dataset, as explained in Sect. 3.2 of the main text, the metrics of the measured/reconstructed PM_{10} concentrations remain similar, with $R^2 = 0.97$, intercept $-0.88 \,\mu\mathrm{g}\,\mathrm{m}^{-3}$ and slope 1.06. All optical absorption and dimensional 'species' show good reconstructions ($R^2 > 0.9$), except for the 6 largest sizes ($R^2 \sim 0.6$).

271 S9 Supporting materials on RASPBERRY results

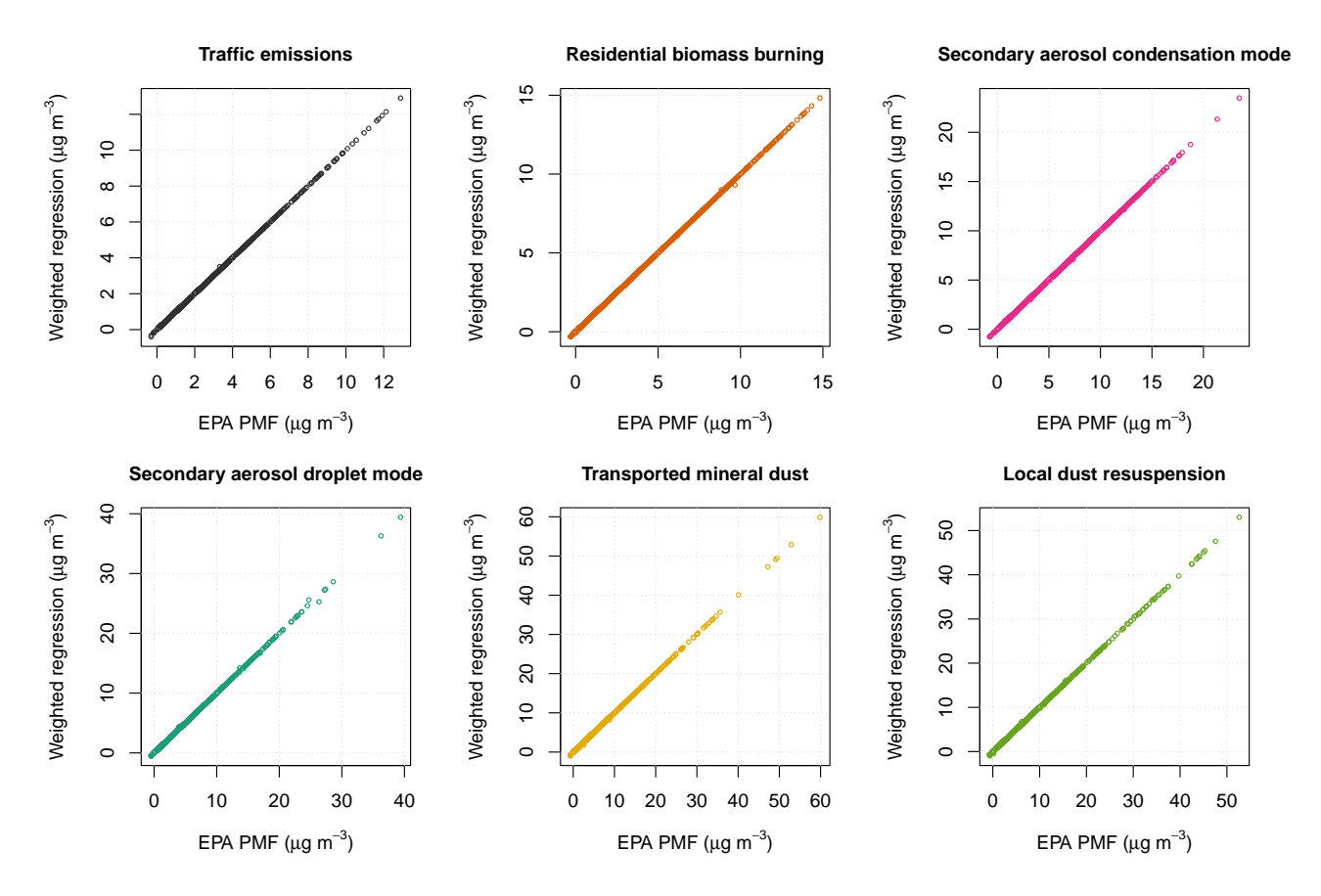


Figure S5: Consistency check of the results obtained using EPA PMF5.0 (x-axis) and the RASPBERRY inversion matrix technique introduced in this study (Eq. 6 in the main text, y-axis), when applying the same profile matrix derived from the PMF. This test considers only the subset of measurements used as input to the PMF. Minor discrepancies are observed, likely attributable to the robust handling of outliers in EPA PMF or numerical approximation errors.

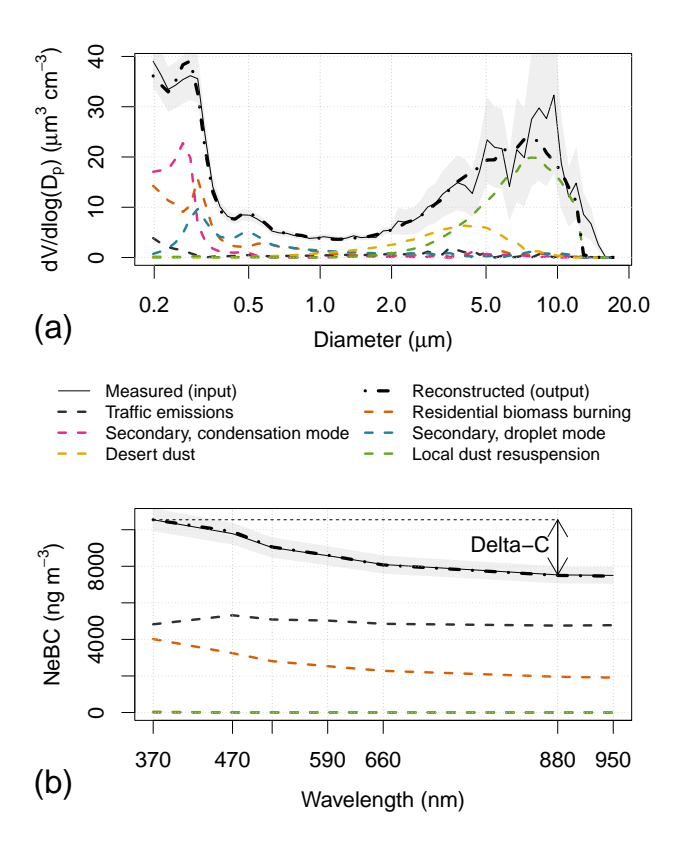


Figure S6: Example of fitting of (a) the volume size distribution measured by the OPC (3 January 2020, 21:30 local time) and (b) the spectral absorption coefficient expressed as NeBC mass, both shown as continuous black lines. The measurement uncertainty provided to the PMF is plotted as a grey band. The coloured dashed lines represent the six factor profiles identified by the physical PMF, weighted such that their sum (dash-dotted line) best fits the measurements. The same weightings are used to calculate the PM₁₀ contributions attributed to each factor. This winter case is here selected because of the high concentrations of both PM₁₀ mass (>60 μ g m⁻³) and NeBC.

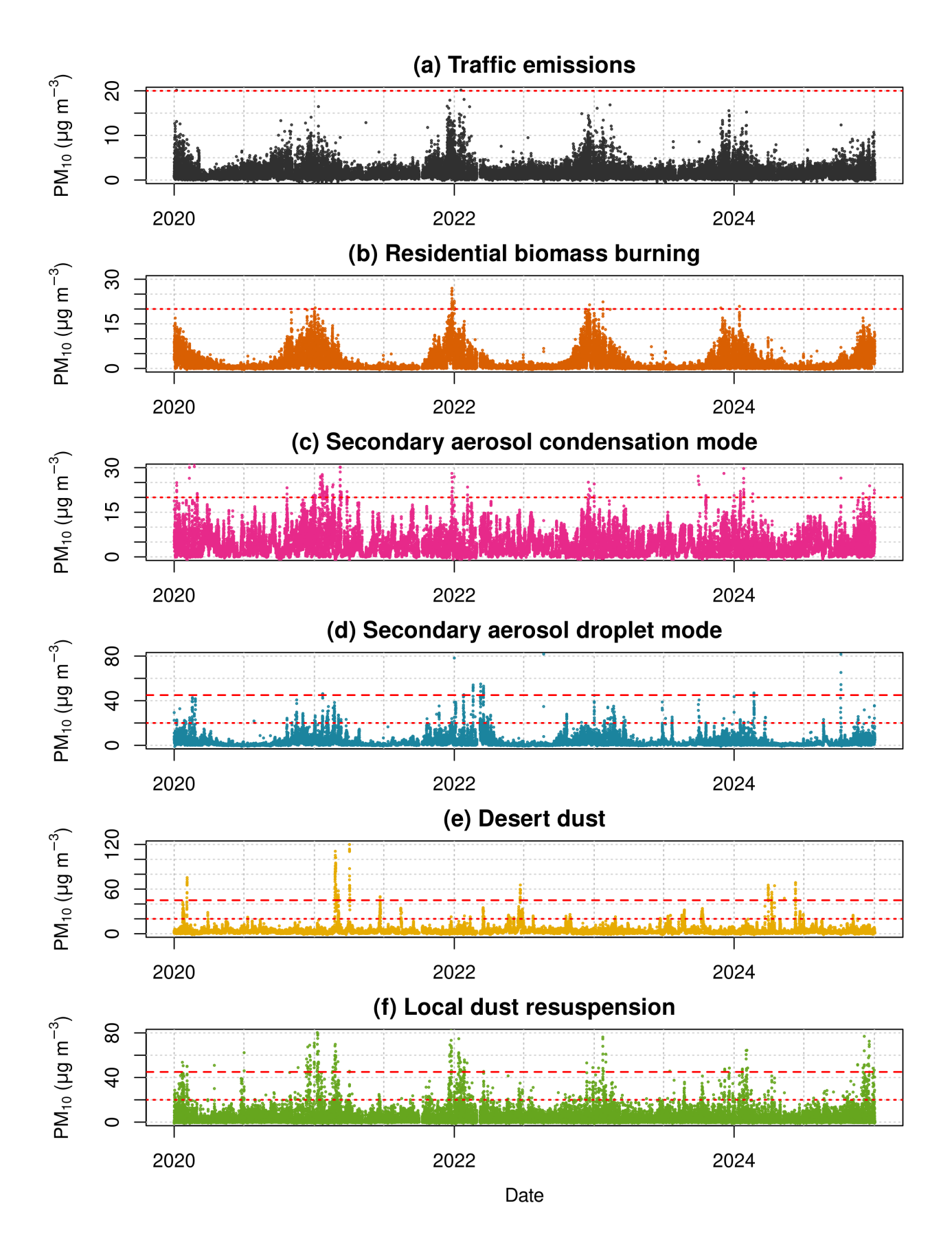


Figure S7: Contribution of each factor to PM_{10} over the entire 2020–2024 period as obtained by RASPBERRY. Red horizontal lines: PM_{10} annual and daily average limit values introduced by the 2024/2881/EC AQ directive.

Table S2: Apparent mass densities of each factor identified by the physical PMF. The uncertainty range is an approximate estimation based on the results of the DISP test, i.e. the $dQ^{max}=4$ range of the total variable (PM₁₀) mean fraction associated to the factor.

Factor	Density (range), $g cm^{-3}$
Traffic emissions	8.9 (8.3–10.1)
Residential biomass burning	3.2 (1.4–3.9)
Condensation mode aerosol	3.6 (3.4 - 4.4)
Droplet mode aerosol	$3.1\ (2.7-3.8)$
Desert dust	$1.3 \ (1.3-1.4)$
Local dust resuspension	0.8 (0.8–0.8)

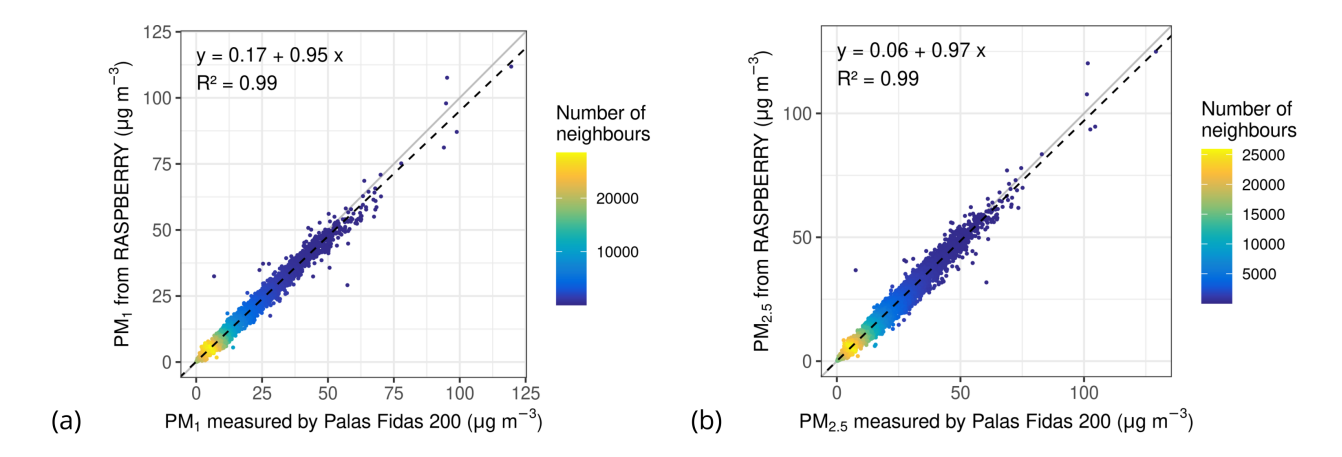


Figure S8: Comparison of measured concentrations (x-axis) and RASPBERRY reconstructions (y-axis) for (a) PM_1 and (b) $PM_{2.5}$. The reconstructed concentrations are calculated similarly to PM_{10} after reassessing the effective densities of the factors, based on their respective maximum diameters (1 and $2.5 \,\mu m$ instead of $10 \,\mu m$). The colour scale represents the density of the points.

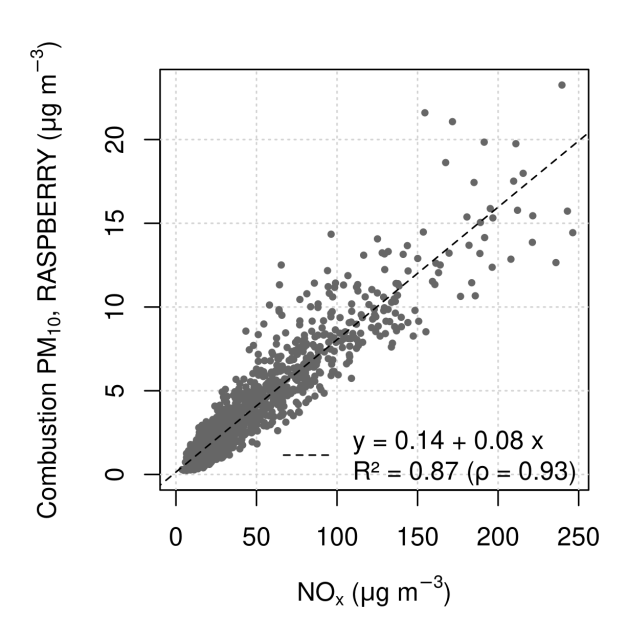


Figure S9: Scatter plot between NO_x (x-axis) measured at Aosta–Downtown and the sum of the PM_{10} contributions from traffic emissions and residential biomass burning determined by RASPBERRY (y-axis).

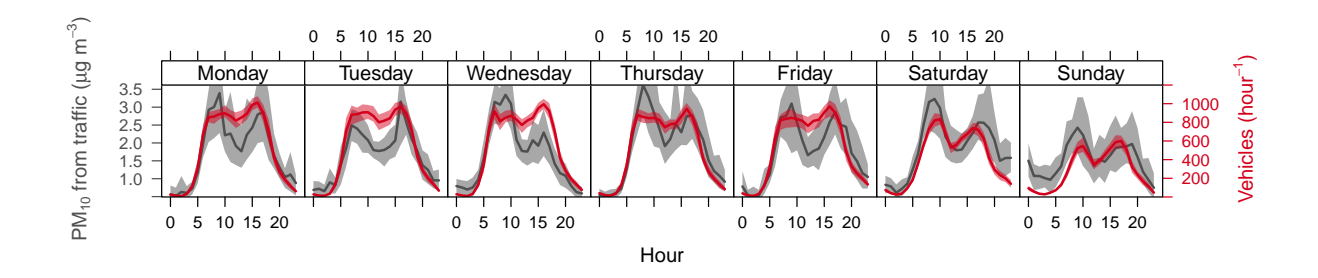


Figure S10: Average daily cycle of PM_{10} concentrations attributed to traffic at Aosta–Downtown (grey, vertical axis on the left) and vehicle counts recorded 500 m to the south (red, vertical axis on the right), during the period 2020–2021. Notice that no meteorological or dilution normalisation was applied to the PM_{10} concentrations.

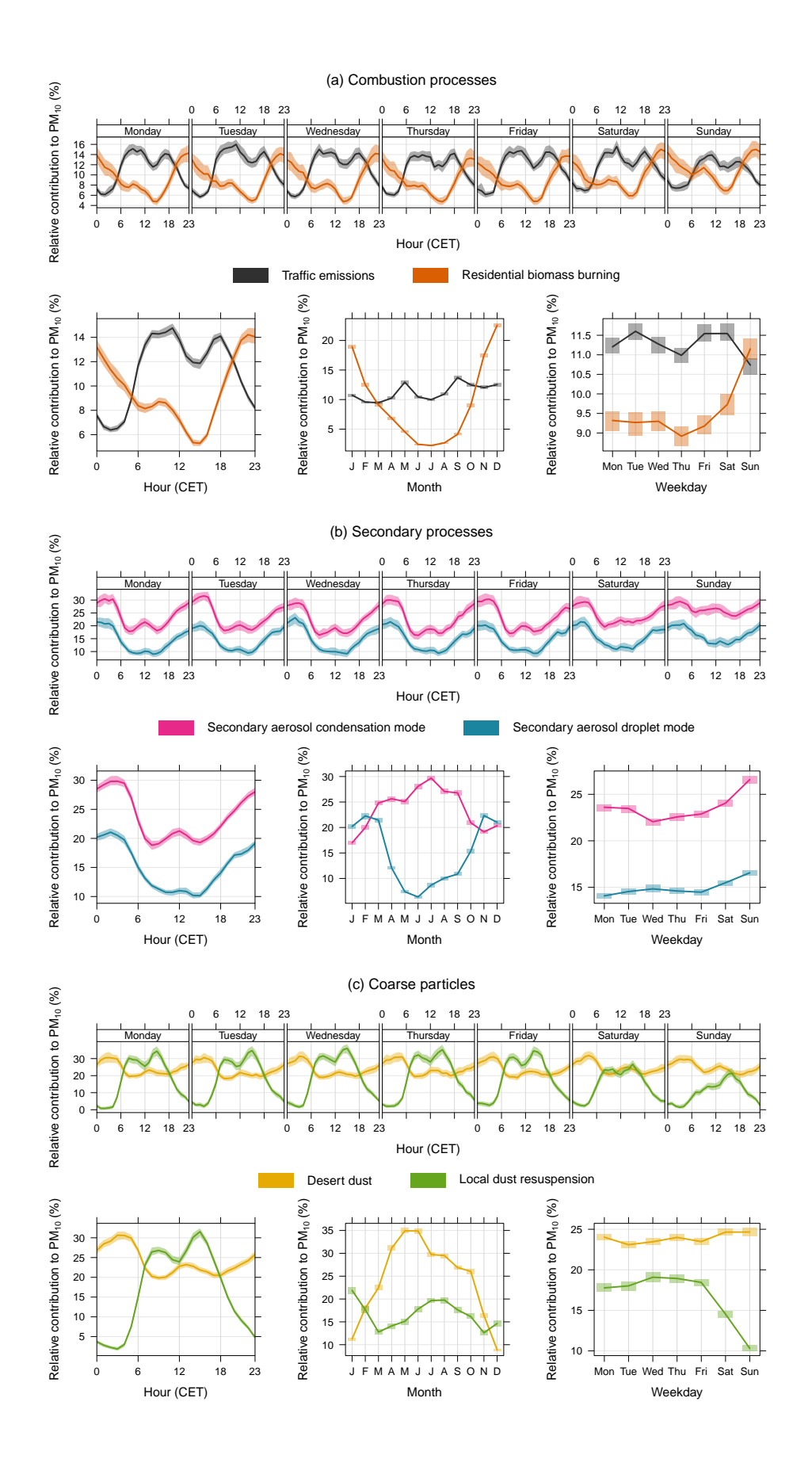


Figure S11: Average percentage contributions to PM_{10} at different temporal scales for factors associated with (a) combustion processes, (b) secondary processes, (c) coarse particles. The bold lines represent the mean contributions, while the coloured areas denote the 95 % confidence interval around the mean.

Combustion processes

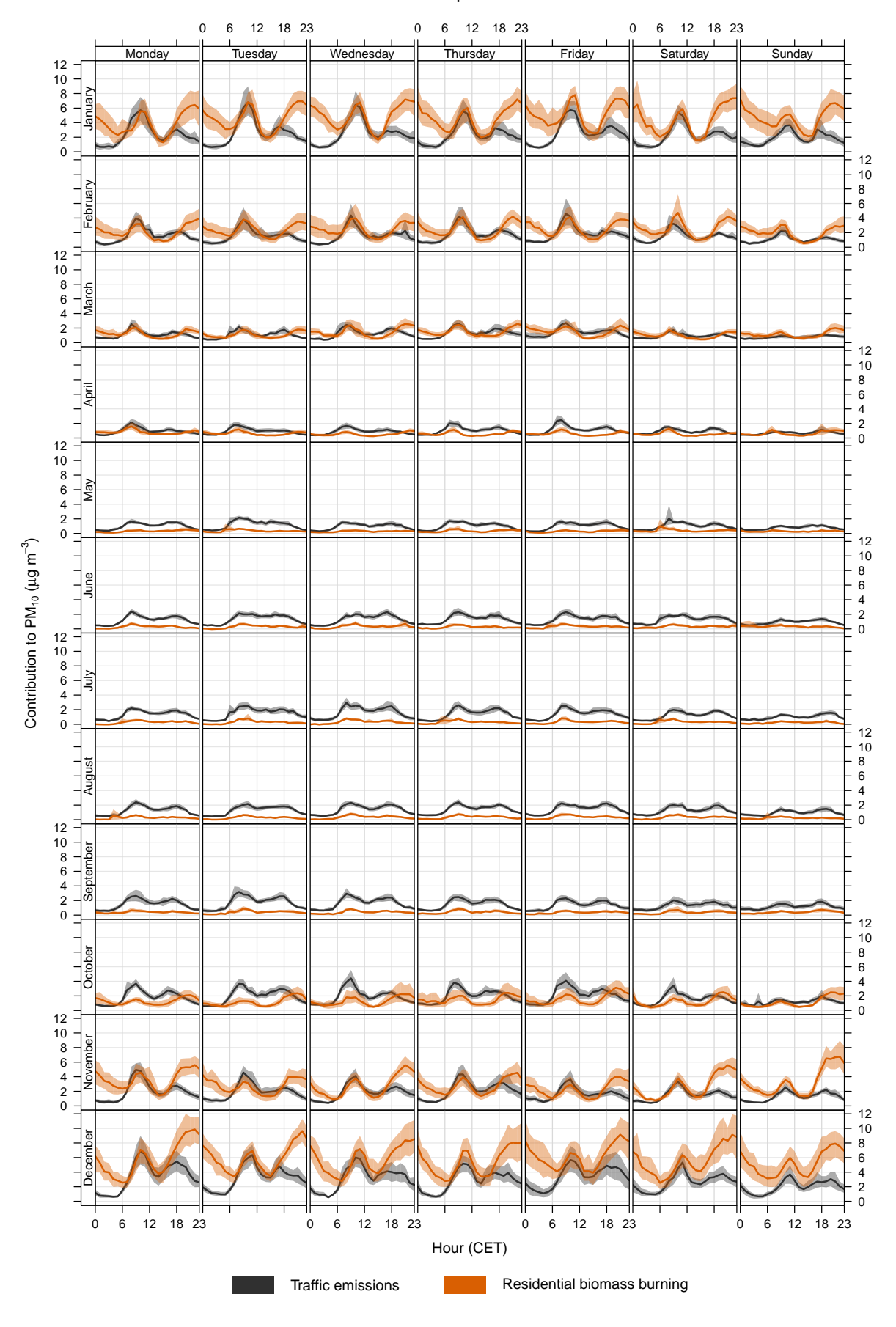


Figure S12: Hourly average contributions to PM_{10} of combustion-related sources split by month and day of the week. The bold lines represent the mean contributions, while the coloured areas denote the 95 % confidence interval around the mean.

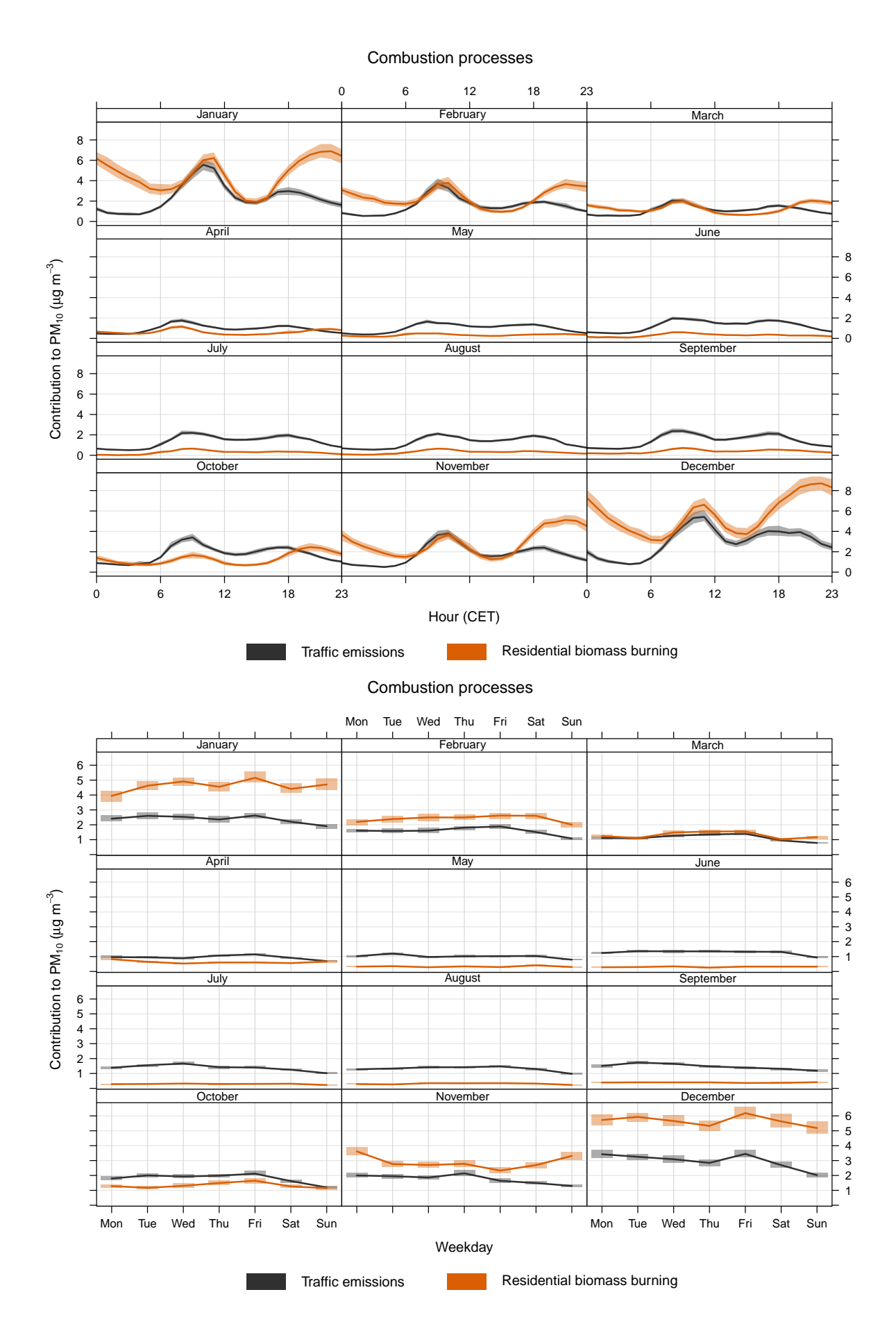


Figure S13: Average contributions to PM_{10} of combustion-related sources split by month as a function of the time of the day and day of the week.

Secondary processes

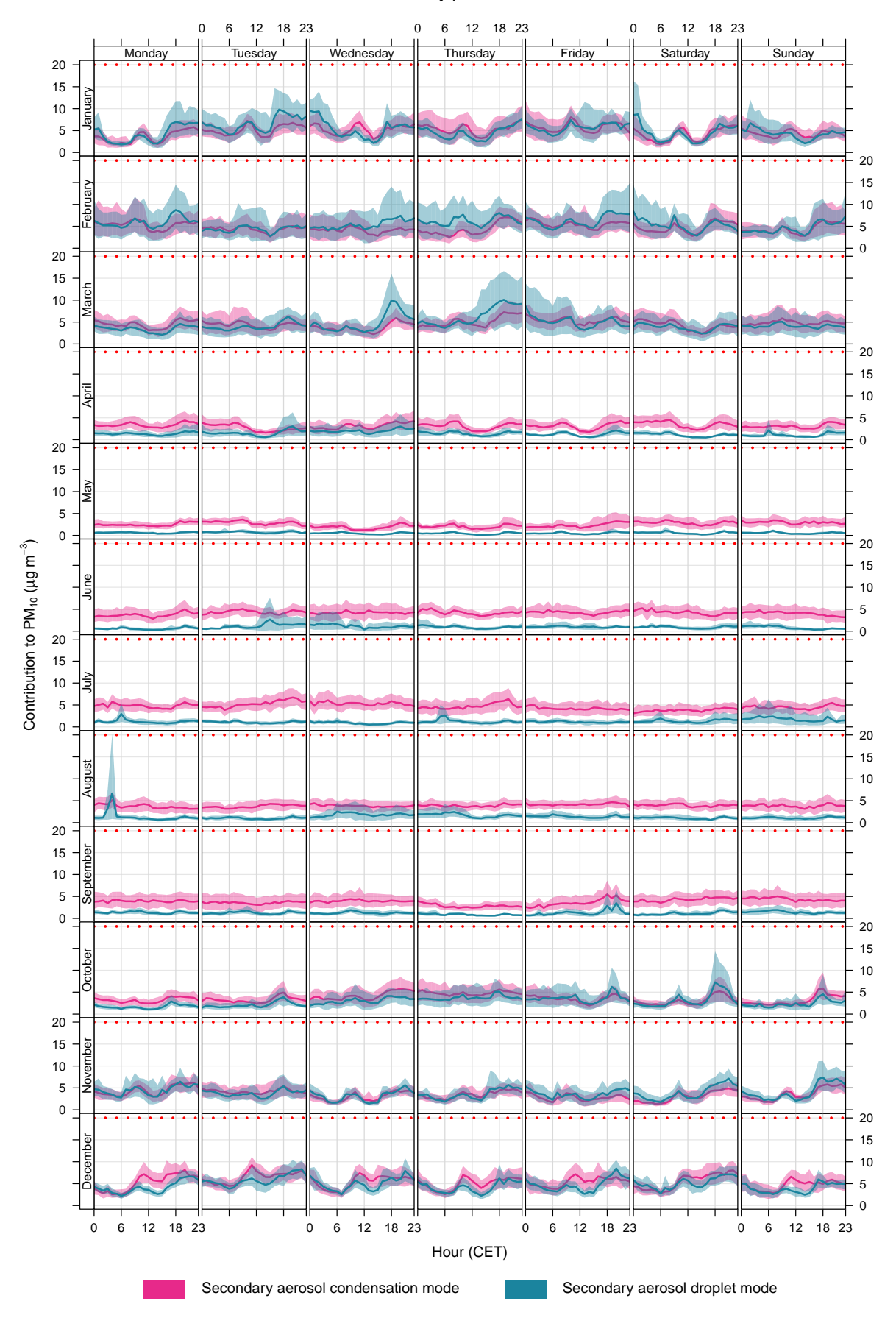


Figure S14: Hourly average contributions to PM_{10} of factors related to secondary particles split by month and day of the week. Red dotted line: PM_{10} (annual average) limit value introduced by the 2024/2881/EC AQ directive plotted as reference.

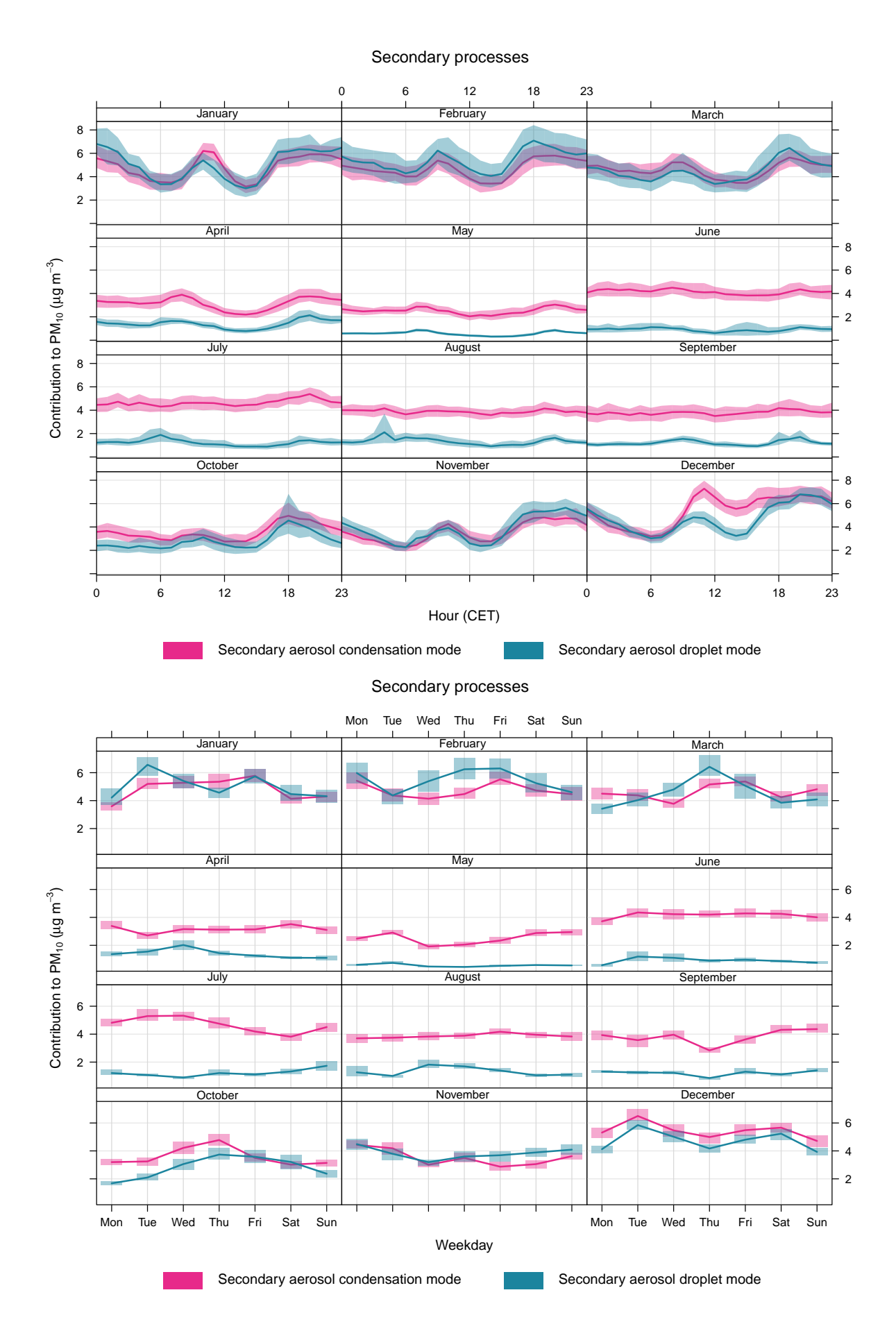


Figure S15: Average contributions to PM_{10} of factors related to secondary particles split by month as a function of the time of the day and day of the week.

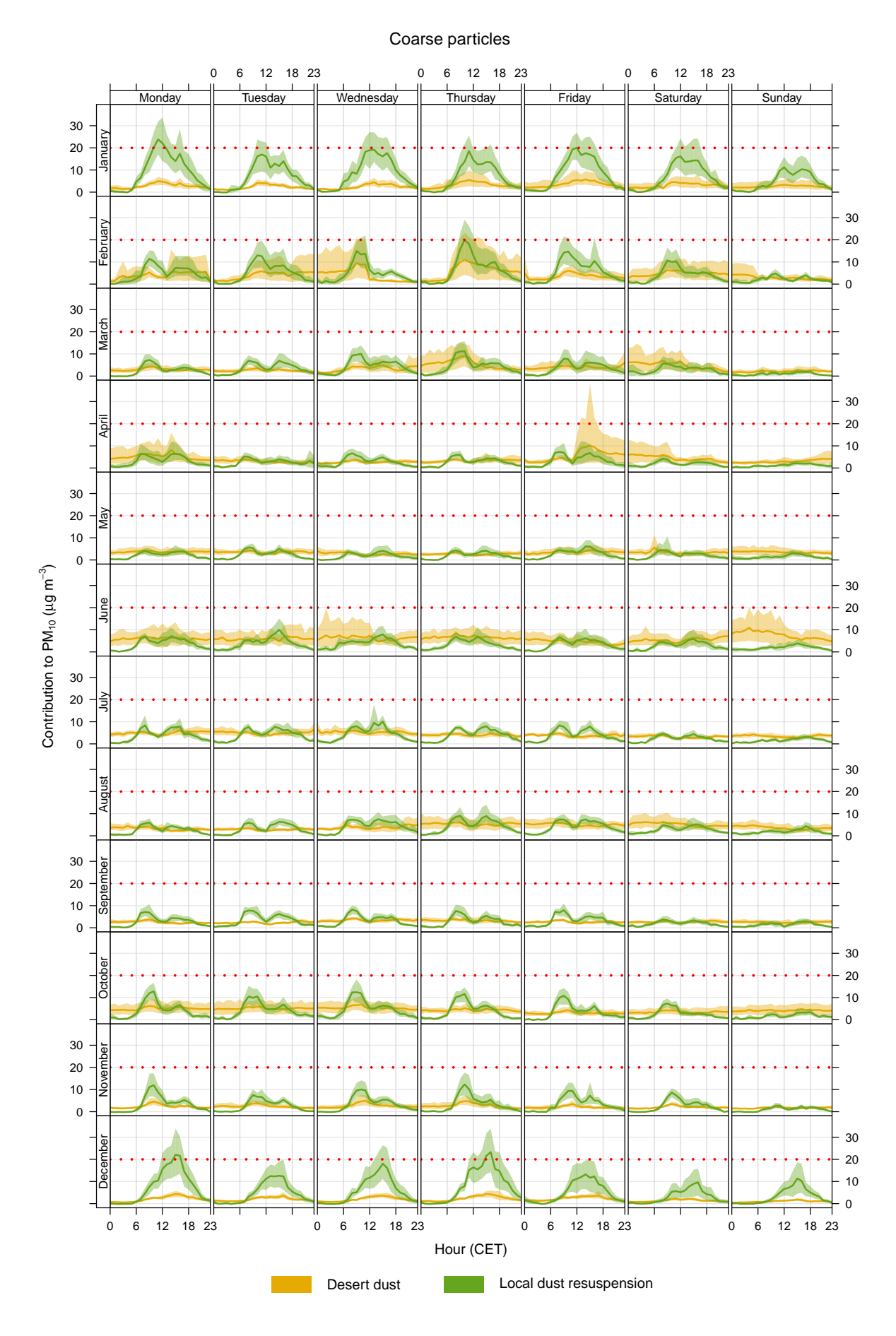


Figure S16: Hourly average contributions to PM_{10} of coarse particles split by month and day of the week. Red dotted line: PM_{10} (annual average) limit value introduced by the 2024/2881/EC AQ directive plotted as reference.

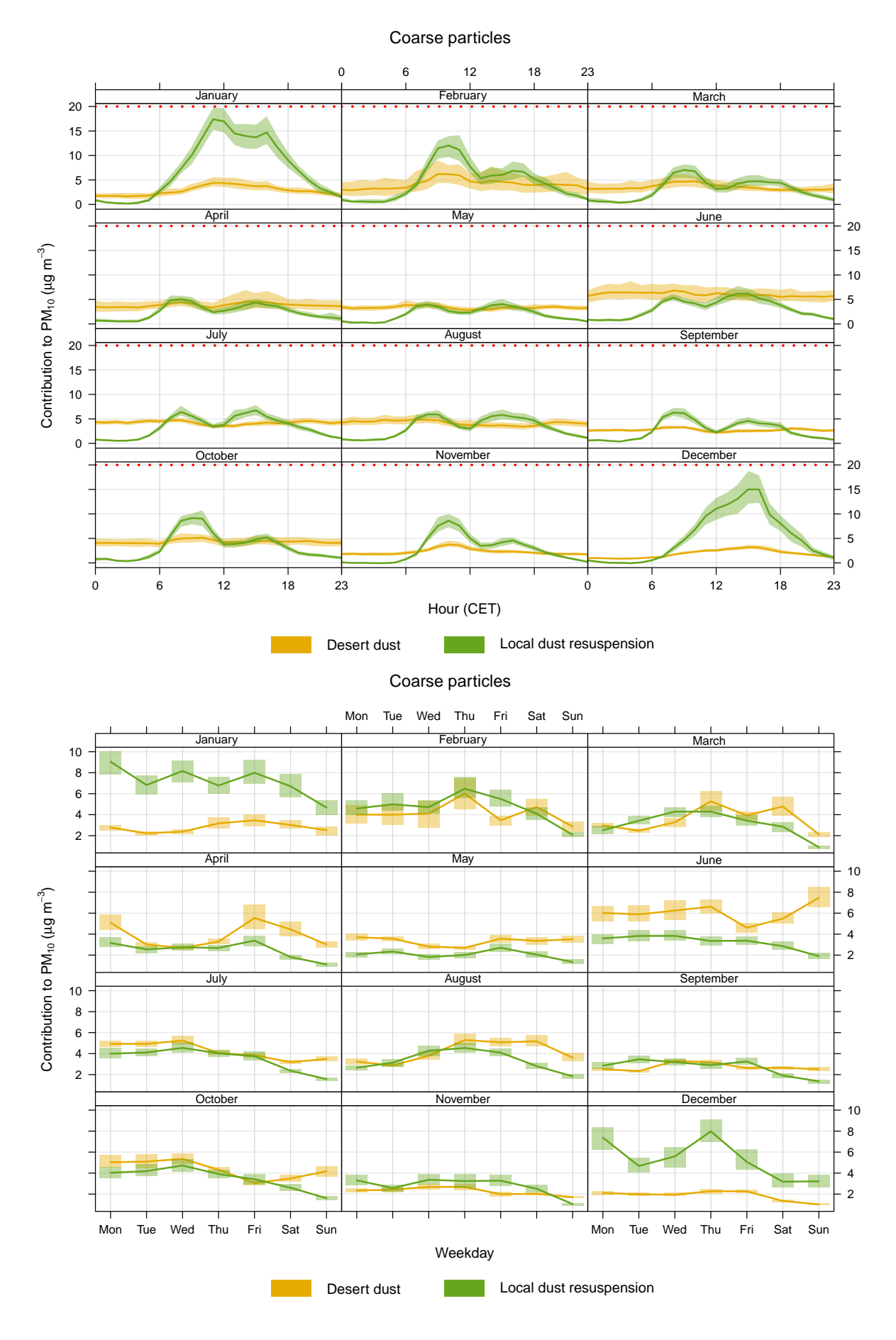


Figure S17: Average contributions to PM_{10} of coarse particles split by month as a function of the time of the day and day of the week. Red dotted line: PM_{10} (annual average) limit value introduced by the 2024/2881/EC AQ directive plotted as reference.

Combustion processes

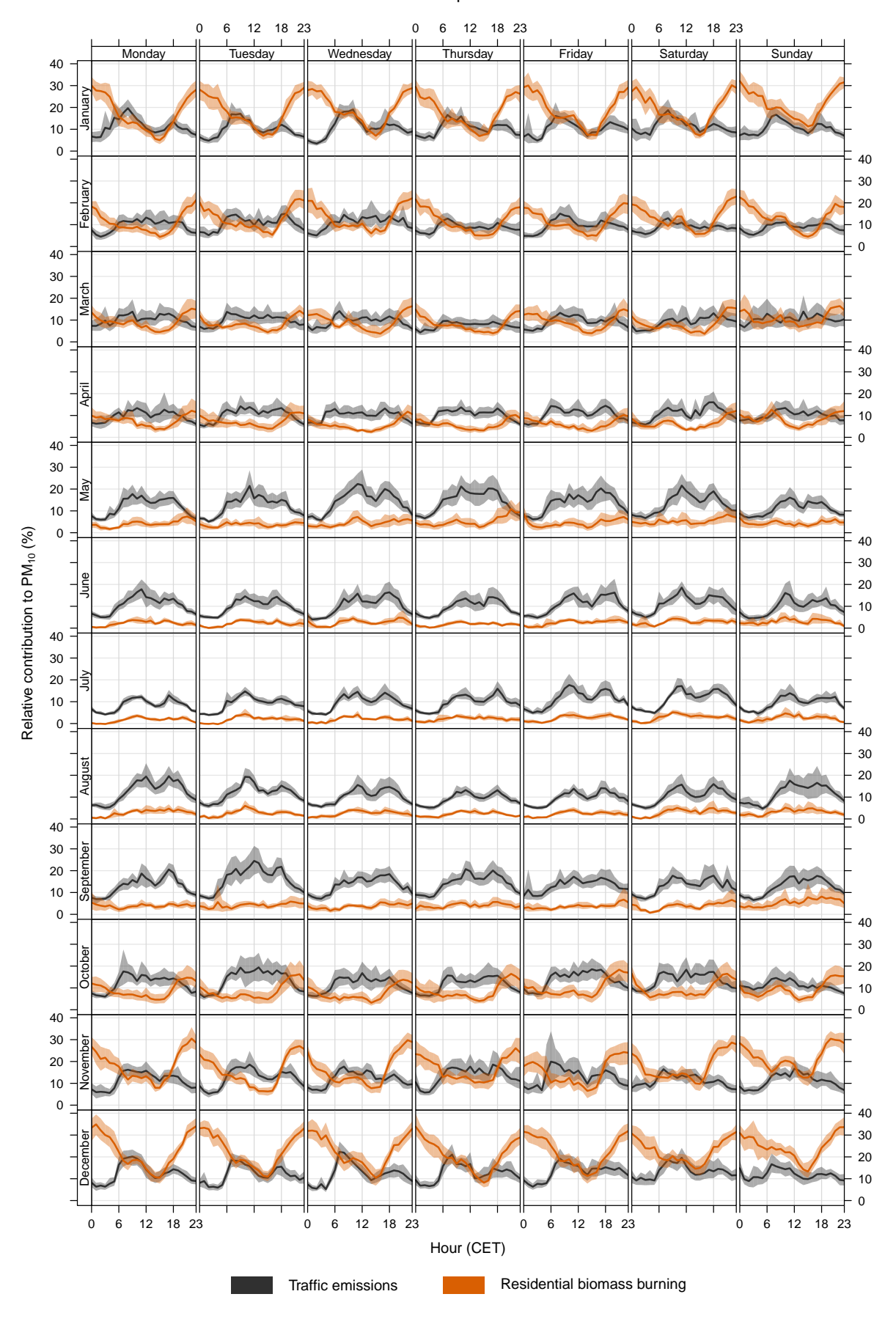


Figure S18: Hourly average percentage contributions to PM_{10} of combustion-related sources split by month and day of the week. The bold lines represent the mean contributions, while the coloured areas denote the 95 % confidence interval around the mean.

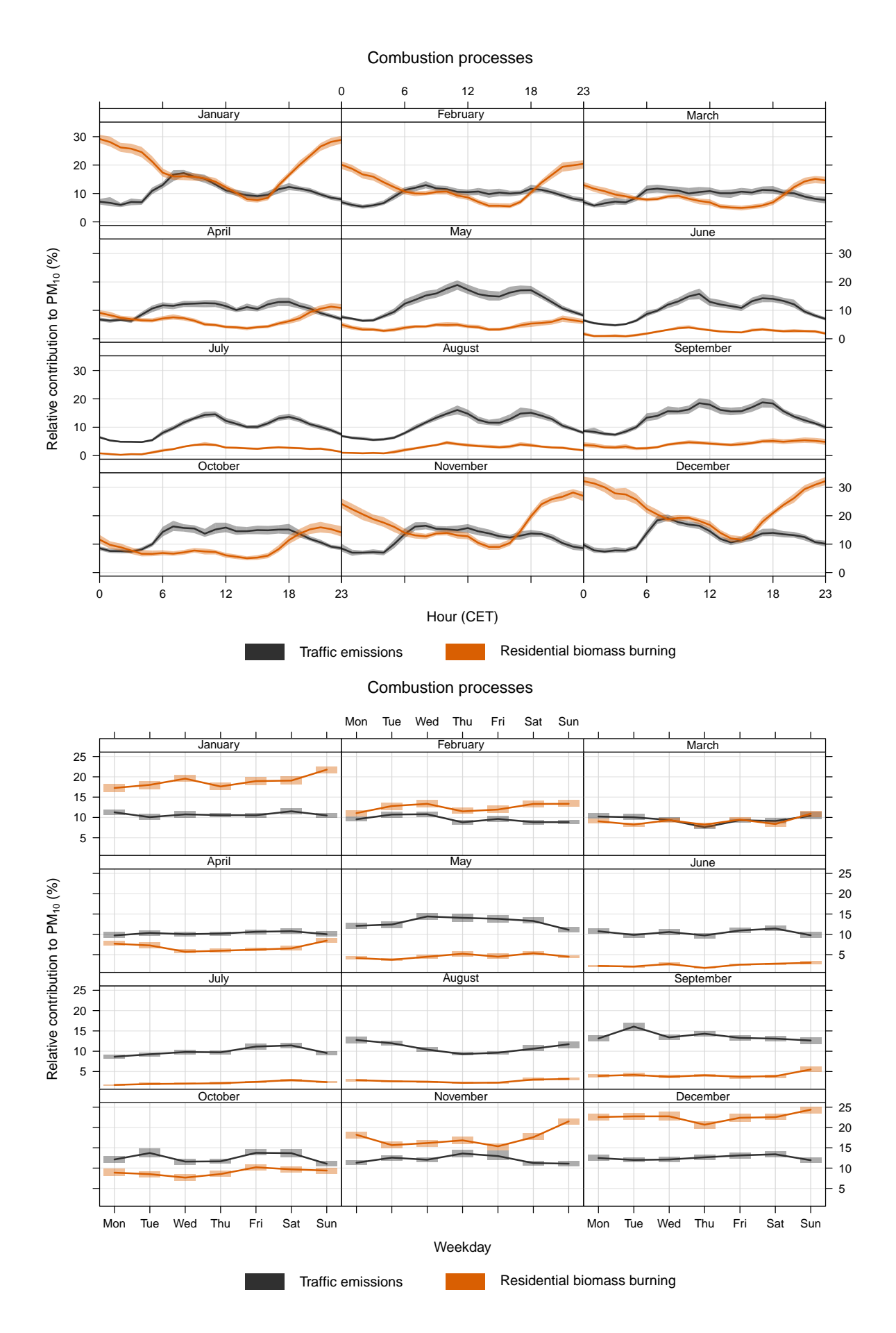


Figure S19: Average percentage contributions to PM_{10} of combustion-related sources split by month as a function of the time of the day and day of the week.

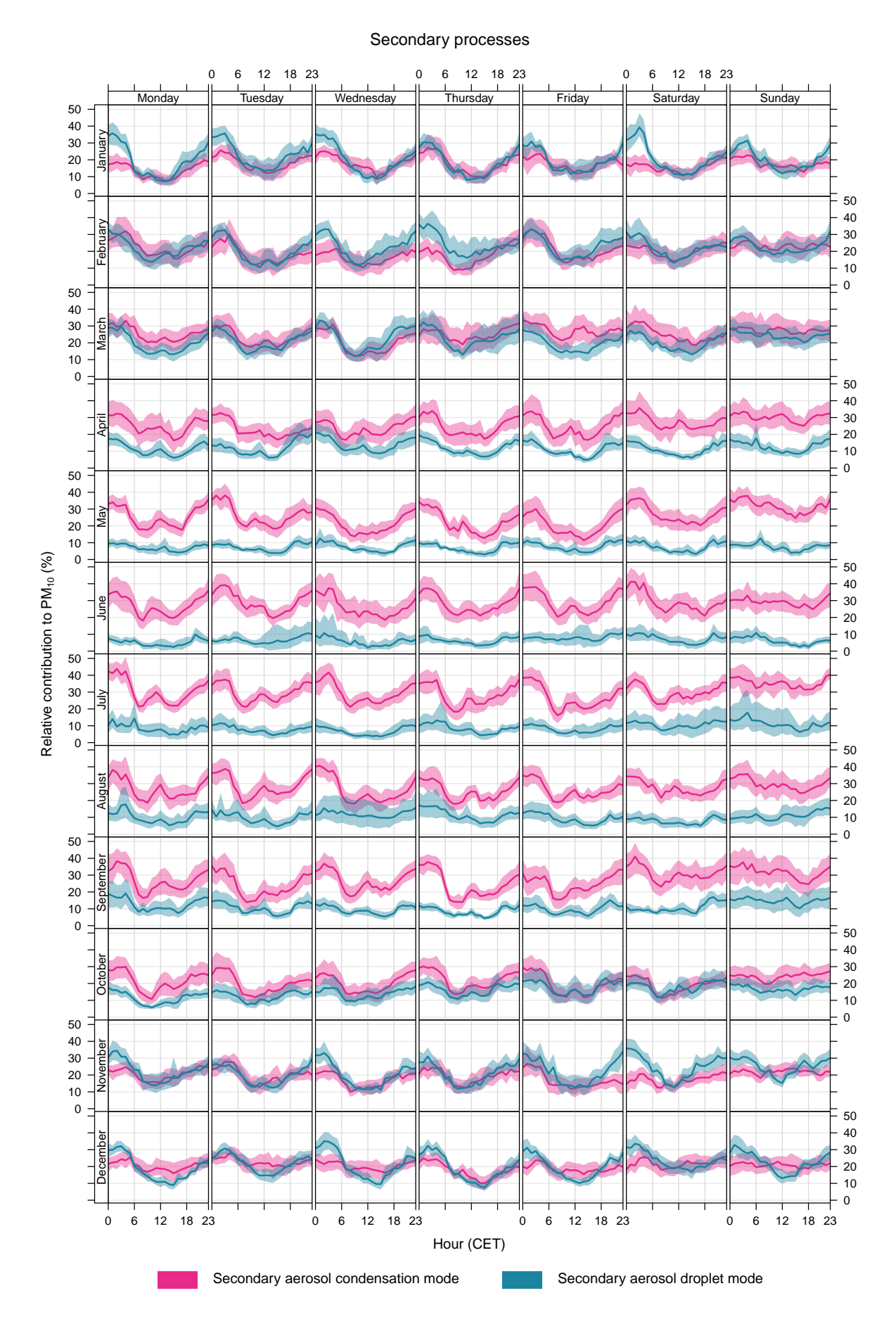


Figure S20: Hourly average percentage contributions to PM_{10} of factors related to secondary particles split by month and day of the week.

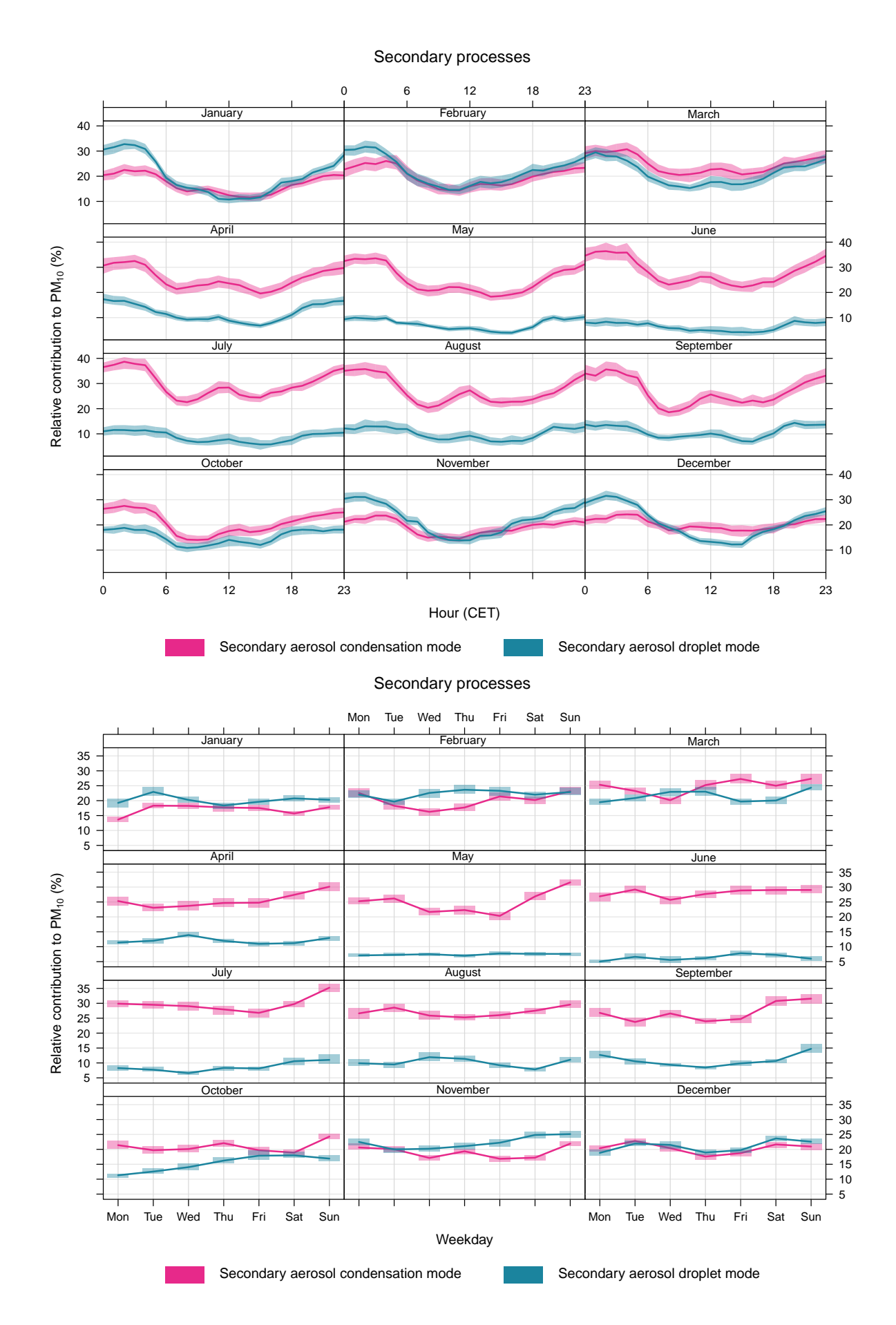


Figure S21: Average percentage contributions to PM_{10} of factors related to secondary particles split by month as a function of the time of the day and day of the week.

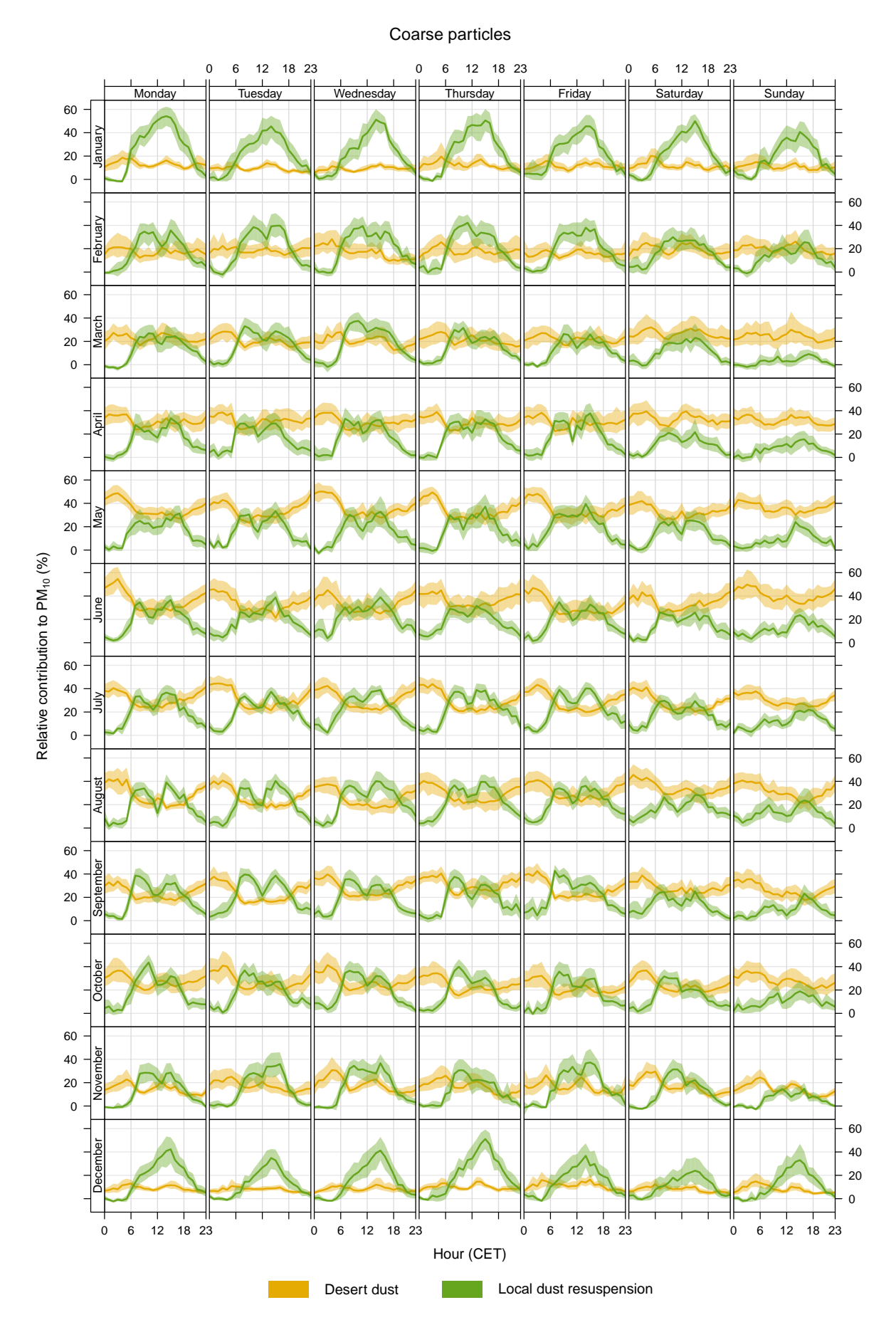


Figure S22: Hourly average percentage contributions to PM_{10} of coarse particles split by month and day of the week.

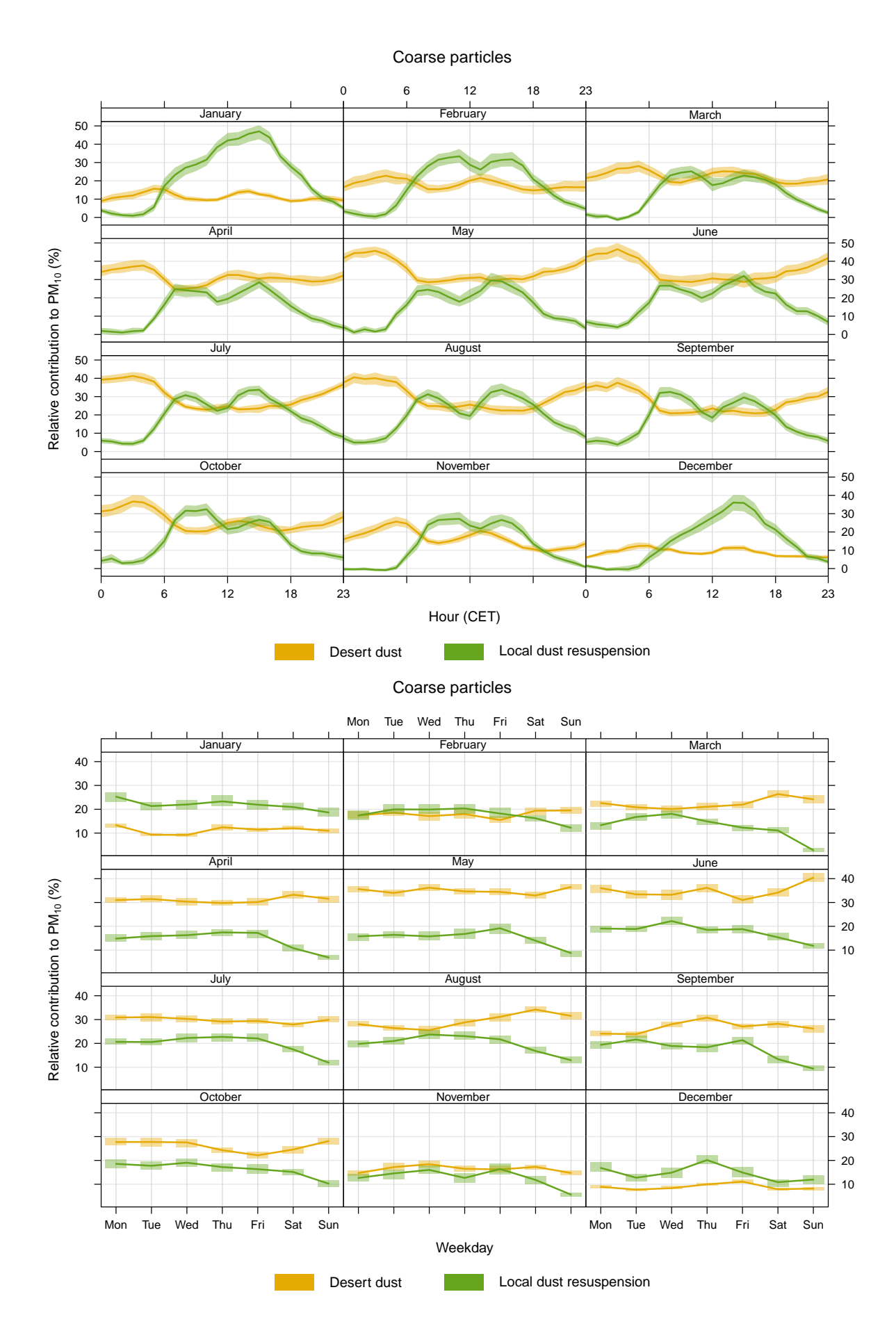


Figure S23: Average percentage contributions to PM_{10} of coarse particles split by month as a function of the time of the day and day of the week.

S10 Examples of desert dust layers aloft and entering the mixing layer

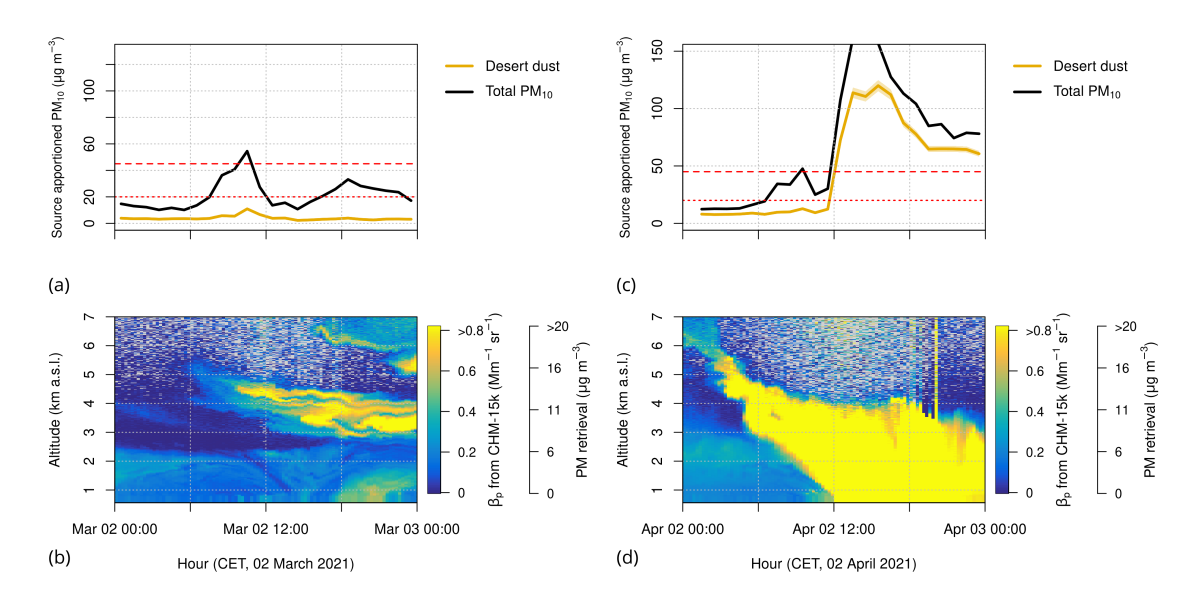


Figure S24: Surface PM attributed to desert dust by RASPBERRY (a, c) and ALICENET PM retrievals along the vertical profile (b, d), based on ALC backscatter measurements and the methodology explained by Bellini et al. (2024). Two representative cases of desert dust transport in 2021, selected from those discussed in the main text, are presented: (a, b) an elevated layer detected by remote sensing instruments (sun photometer and ALC) throughout the atmospheric column but not observed by surface-level instruments; (c, d) a dust layer reaching the surface and significantly affecting local air quality.

S11 HYSPLIT configuration and concentration-weighted trajectories

The HYSPLIT model (Stein et al., 2015; Rolph et al., 2017) is employed to generate 7-day back-trajectories every 6 hours over the entire 2020–2024 period (for a total of more than 7,000 trajectories), based on wind fields from the Global Data Assimilation System (GDAS) at 1° resolution. The trajectory endpoints are set to the coordinates of Aosta at an altitude of 1500 m a.g.l., identified as a representative altitude for both long-range transport and entrainment processes to the surface. For the CWT field calculations, only trajectory points sufficiently close to the surface are considered. Based on the examination of mixing height outputs from the GDAS model and scientific literature (e.g., Barreto et al., 2022), the maximum altitude was set to 2000 m a.g.l. in winter, 4000 m a.g.l. in spring and autumn, and 6000 m a.g.l. in summer.

S12 Coarse particle resuspension and depolarisation ratio from the automated lidar-ceilometer

284

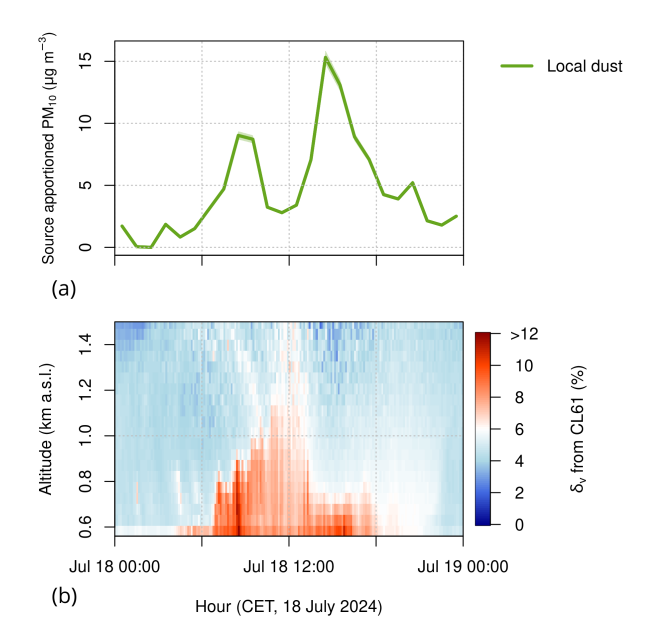


Figure S25: Example of the relationship between (a) PM_{10} surface contributions from coarse particles, as derived from RASPBERRY, and (b) the evolution of the volume depolarisation vertical profile measured by the CL61 on a typical summer day (18 July 2024). The colour scale limits in the bottom plot have been tweaked to enhance the contrast between conditions of low aerosol backscatter or spherical-shaped particles (low depolarisation) and the presence of irregularly shaped particles in the atmosphere (high depolarisation).

S13 Supporting materials on the comparison between chemical PMF and RASPBERRY

286

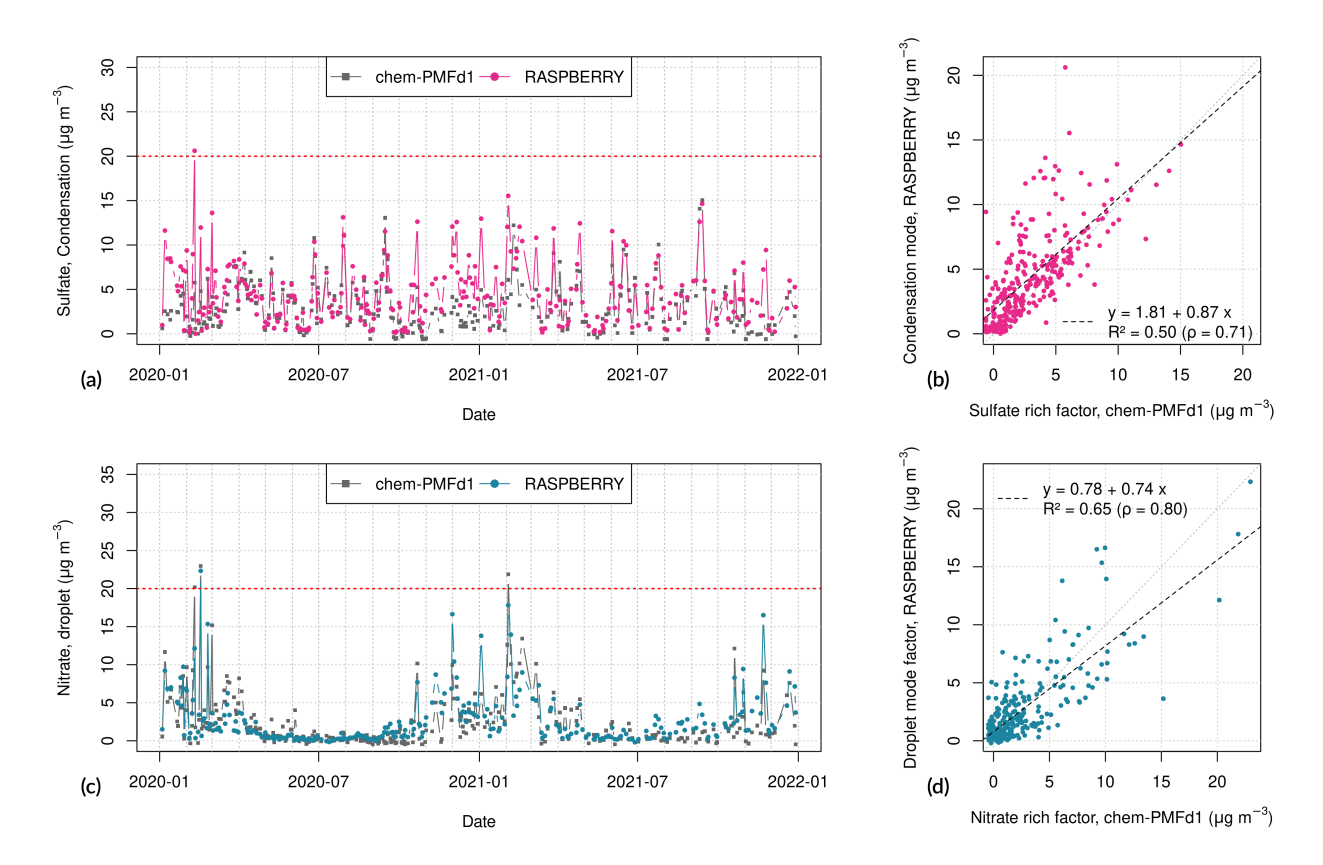


Figure S26: Comparison of PM₁₀ source contributions derived from the chemical PMFs (dataset 1, with anion, cation, EC/OC and levoglucosan) and RASPBERRY, presented using time series plots (a, c) and scatter plots (b, d) with regression equations displayed within the plots. Both plot types include only samples from coincident dates across both datasets, limiting the comparison to the subperiod 2020–2021. Specifically: (a–b) represent the contribution from the sulfate-rich factor (chemical PMF) and the condensation mode factor (RASPBERRY); (c–d) represent the contribution from the nitrate-rich factor (chemical PMF) and the droplet mode factor (RASPBERRY). Red horizontal line: PM₁₀ (annual average) limit value introduced by the 2024/2881/EC AQ directive plotted as reference.

287 S14 Dependence on wind

288

290

291

292

293

294

295

296

297

298

299

300

301

302

303

304

305

306

307

308

309

310

311

312

313

314

315

316

317

318

319

320

321

322

323

324

325

326

327

328

329

330

331

332

333

334

335

336

Hourly contributions to PM₁₀ from RASPBERRY, unlike daily averages from the chemical PMF, enable correlation with high temporal resolution meteorological data. In this study, we focus on surface wind measurements as they are highly related to PM modulations at the considered site. Ideally, wind data should be obtained from the same location as the aerosol measurements. However, at the Aosta–Downtown station, wind measurements are significantly influenced by the surrounding urban landscape due to the presence of tall buildings. Therefore, for this analysis, wind data from additional stations are used: Aosta–southwest station (approximately 2 km away), Aosta–Saint-Christophe and Aosta–Industrial (on the top of the steel mill). As an example, Fig. S27 presents a conditional probability function (CPF, Ashbaugh et al., 1985) polar plot that combines factor contributions with wind direction and speed measured at the Aosta–southwest station. The colours indicate the ratio of measurements within a wind speed/direction bin when concentrations exceed the 75th percentile to the total number of measurements in that bin. Additionally, Figs. S28–S30 provide similar plots further disaggregated by season, and include wind data from all meteorological stations. It is important to note that, due to a slight change in the orientation of the main valley west of Aosta, northeasterly winds at the Aosta–southwest station correspond to easterly winds at the Aosta–Saint-Christophe station.

The figures generally confirm our earlier source-factor attributions. The highest contributions from traffic emissions at Aosta-Downtown occur in conjunction with low to moderate wind speeds blowing from the northeastern sector relative to Aosta-southwest (Fig. S27a). Notably, the annual polar plot exhibits a bimodal distribution, with two distinct clusters corresponding to the cold (lower wind speeds) and warm (higher wind speeds) seasons, illustrated more clearly in Figs. S28a–S30a. This pattern likely reflects the local origin of urban traffic emissions during winter, with contributions from the eastern part of the city during the warmer months. The latter may be attributed to higher vehicular density in that area and to traffic-polluted air masses advected from the east, perhaps originating from the eastern side of the region (motorway) or even the Po Basin. The biomass burning factor is associated with calm wind conditions (Fig. S27b), which can be explained by the local origin from the city and its surrounding areas, but also with the generally weak winds prevailing in winter, when biomass burning concentrations peak. Conversely, the condensation mode factor shows its highest contributions in correspondence with stronger easterly winds, which is consistent with the expected contribution of secondary particles transported from the Po Basin (Diémoz et al., 2019). A dependence similar to biomass burning is also observed for the droplet mode factor (Figs. S27d and S28d), which exhibits maximum concentrations during calm conditions with a slight bias towards the eastern sector. However, when wind data from Aosta–Saint-Christophe are used instead of Aosta–southwest, this factor demonstrates a clearer dependence on easterly flows (Fig. S29d), supporting the role of air masses advected from the Po Basin. The polar plot for the dust component (Fig. S27e) reveals a dominance of easterly flows (Fig. S27e). This likely reflects the most frequent surface wind direction during dust events rather than the actual provenance of the air masses, already explored in Sect. 4.2.3 and Fig. 7c. Nevertheless, advection from the Po basin could be partly responsible for transporting 'polluted dust' resulting from entrainment and mixing in the lower atmospheric layers of the Po Valley (crustal elements are present in the sulfate-rich chemical factor, suggesting the potential role of such processes, Figs. S3–S4). Finally, it is noteworthy that local coarse particles (Fig. S27f) are mainly associated with very high wind speeds, originating from both the eastern and western sectors. Unlike other factors, local coarse particles show increased contributions even during westerly flows, including foehn winds typically leading to a drop in the concentrations of most pollutants. This phenomenon occurs due to particle resuspension caused by strong winds, regardless of their provenance direction. Near the city centre, the maximum concentration is found in correspondence to southeasterly winds (Fig. S30f), which may be conducive of coarse particle transport from the steel mill to the Aosta-Downtown station. Indeed, as shown in Fig. S31, the CPF maximum clearly points towards the steel mill. Another probable source in this direction is the large parking lot of the cable car departure, which experiences particular crowding during winter.

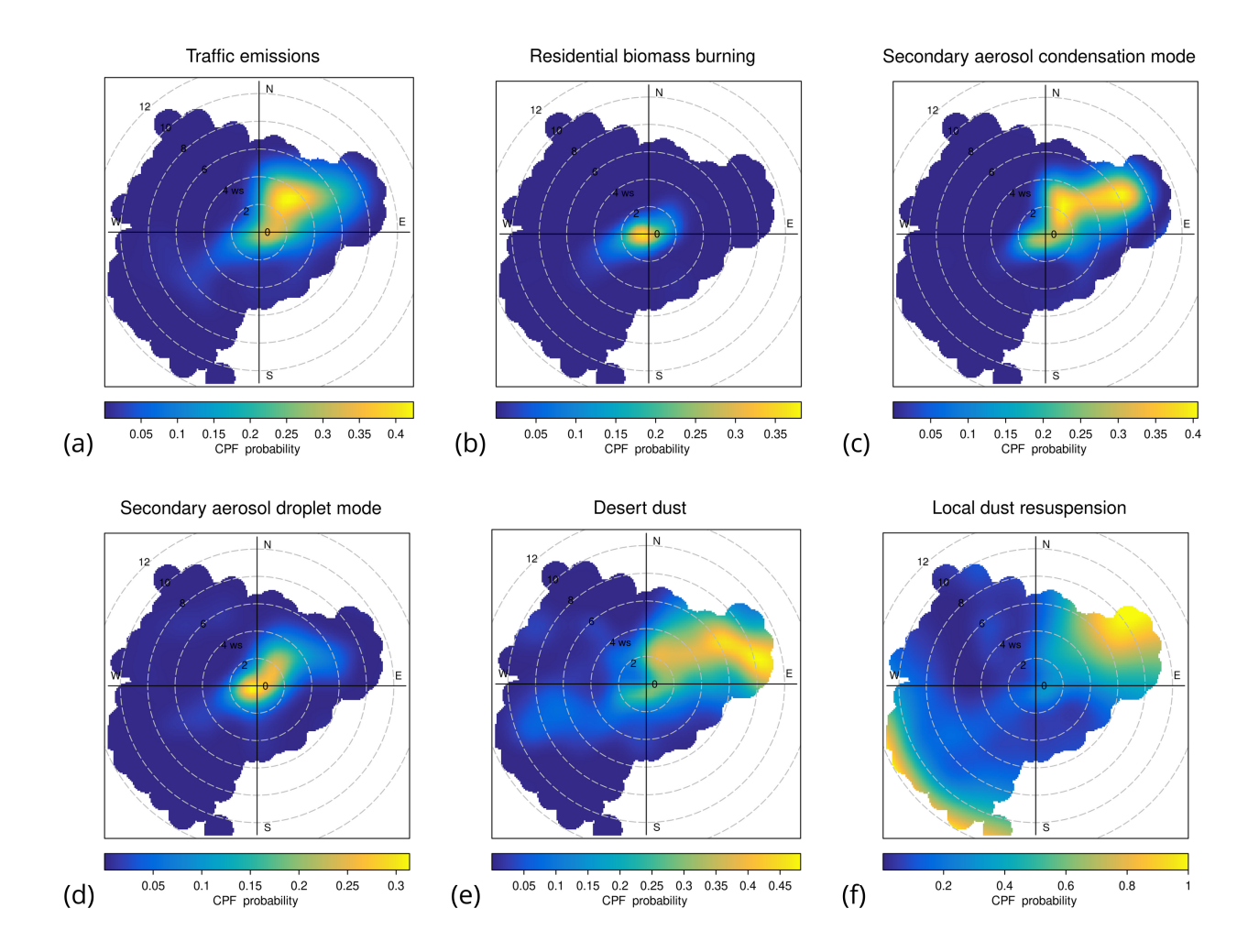


Figure S27: Conditional probability functions for PM_{10} contributions from each factor of RASPBERRY. Data are binned by wind speed (represented as the radial distance from the centre of the plot) and wind direction (polar angle). Colours indicate the ratio of measurements in a bin with concentration exceeding the 75th percentile to the total number of measurements in that bin (Ashbaugh et al., 1985).

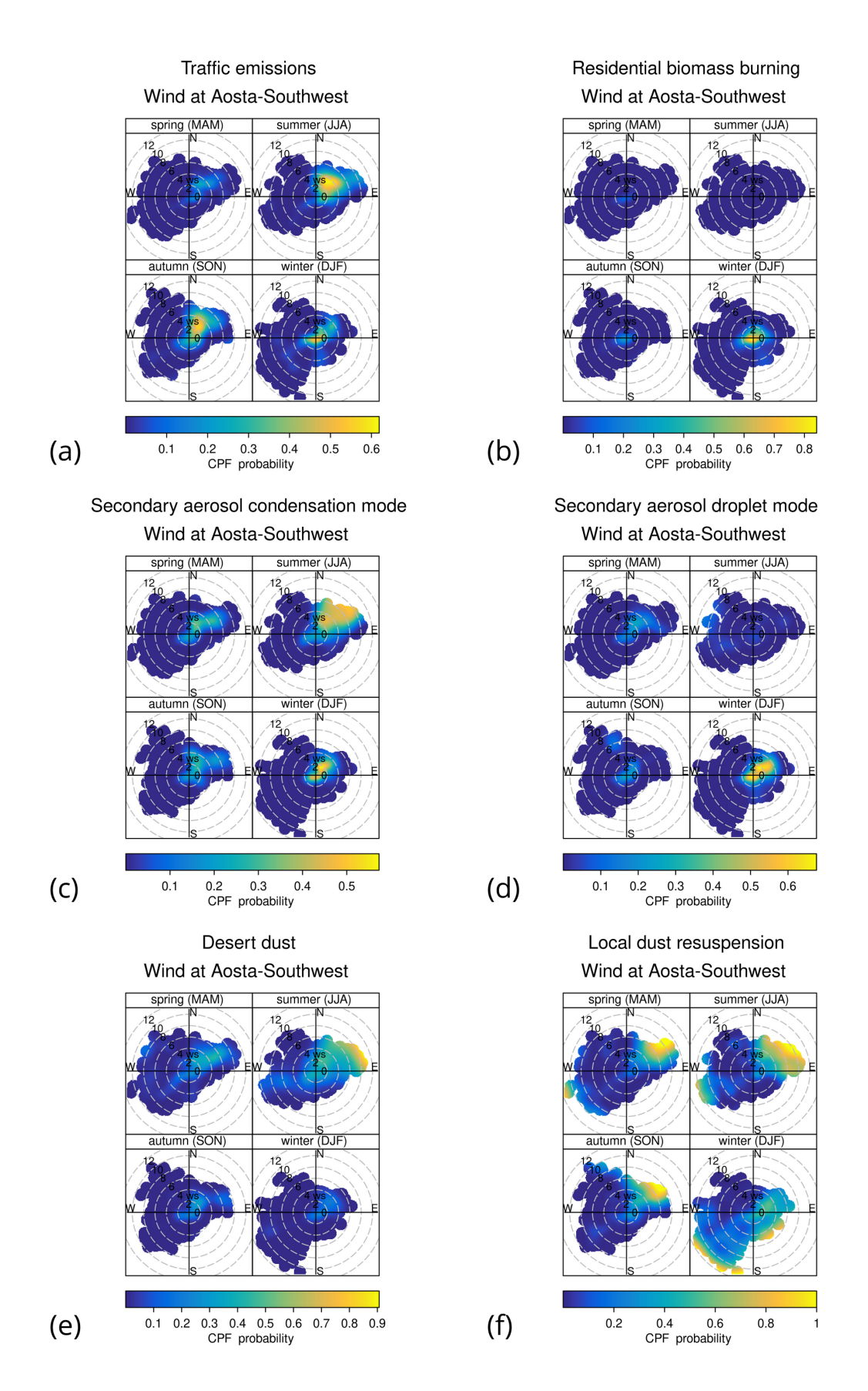


Figure S28: Conditional probability function at the 75th percentile split by season for all emission factors. Wind is taken from the Aosta–southwest station.

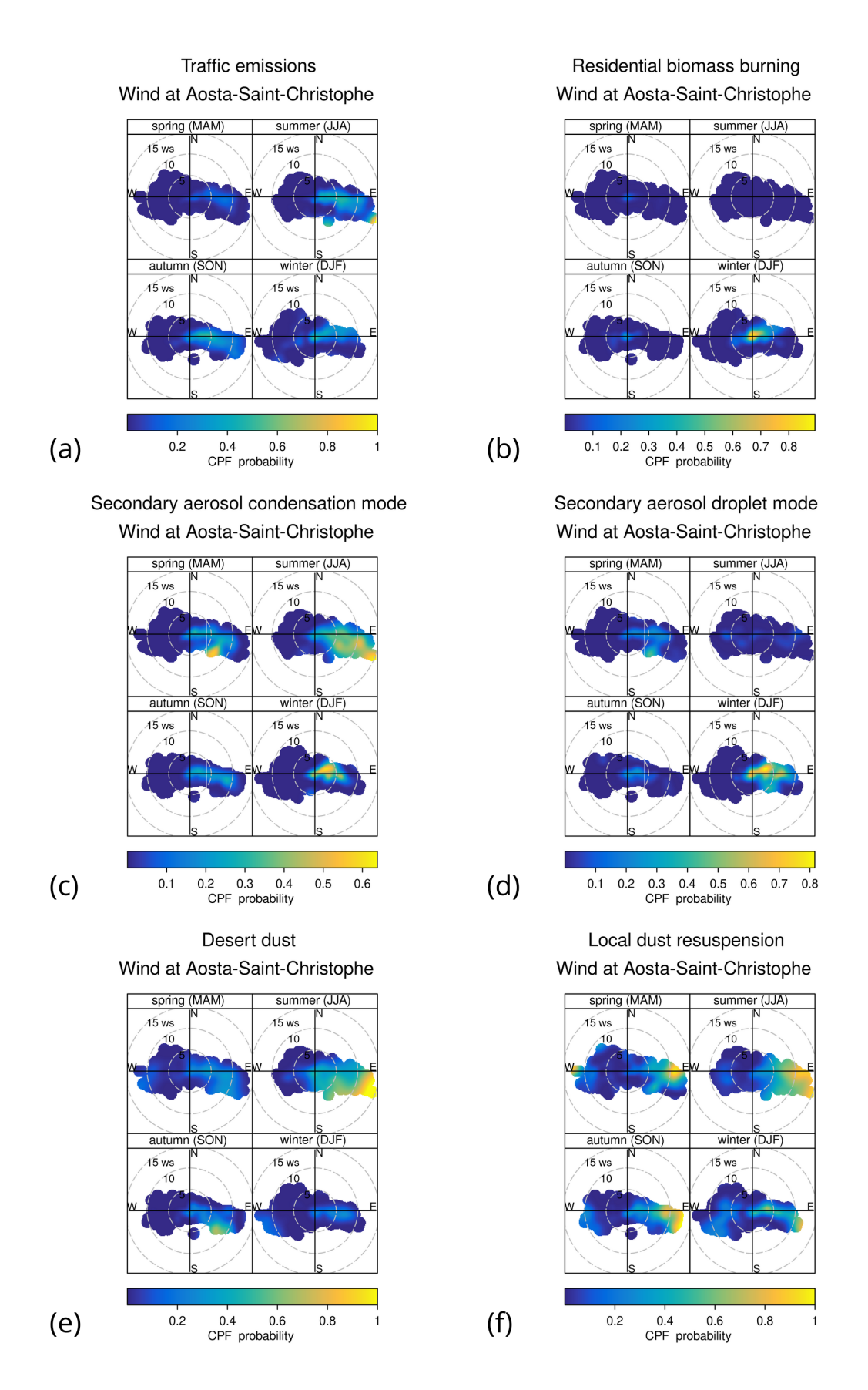


Figure S29: Conditional probability function at the 75th percentile split by season for all emission factors. Wind is taken from the Aosta–Saint-Christophe station.

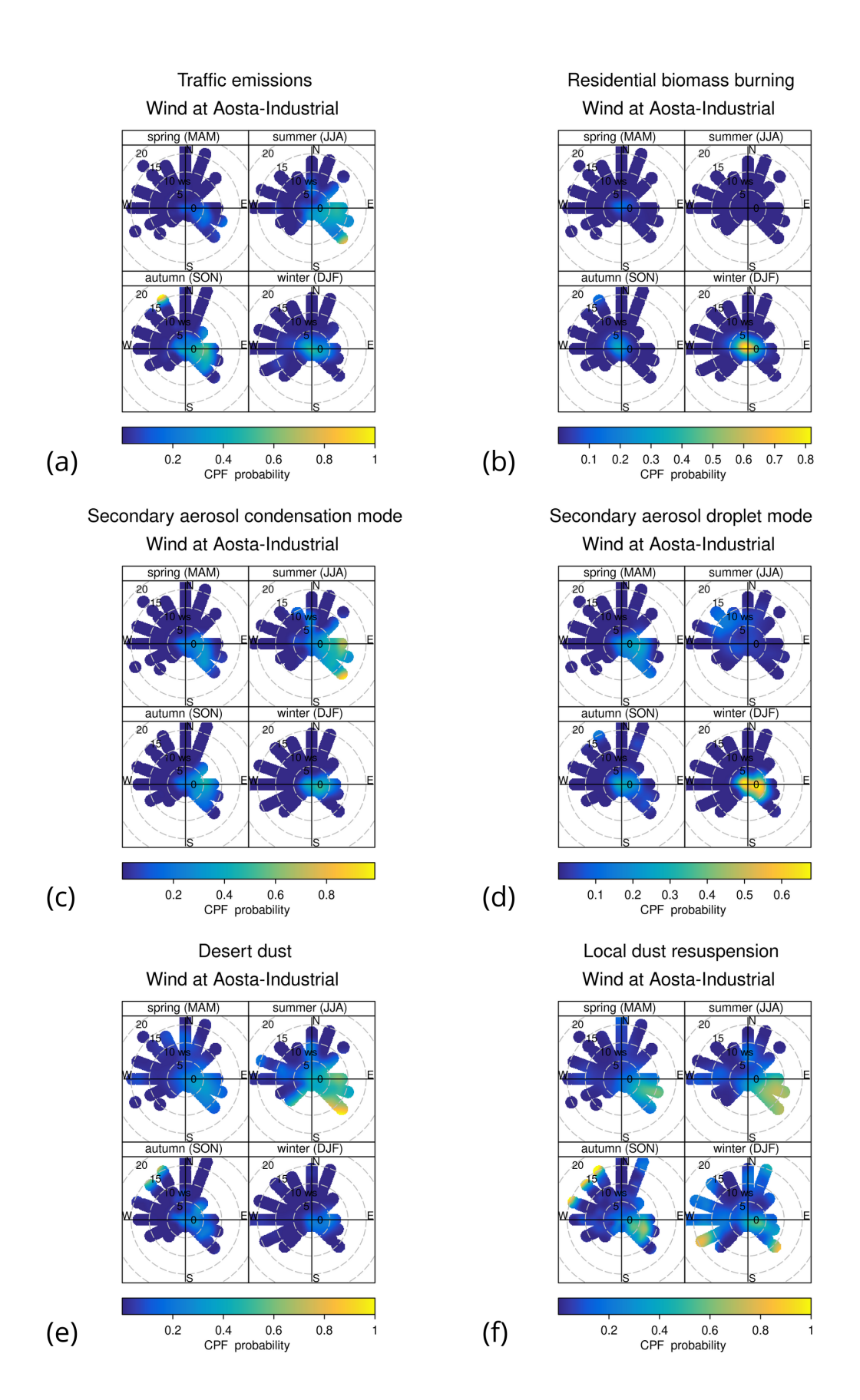


Figure S30: Conditional probability function at the 75th percentile split by season for all emission factors. Wind is taken from a meteorological station installed on the root of the steel mill. In this case, directions are recorded at discrete angular intervals.

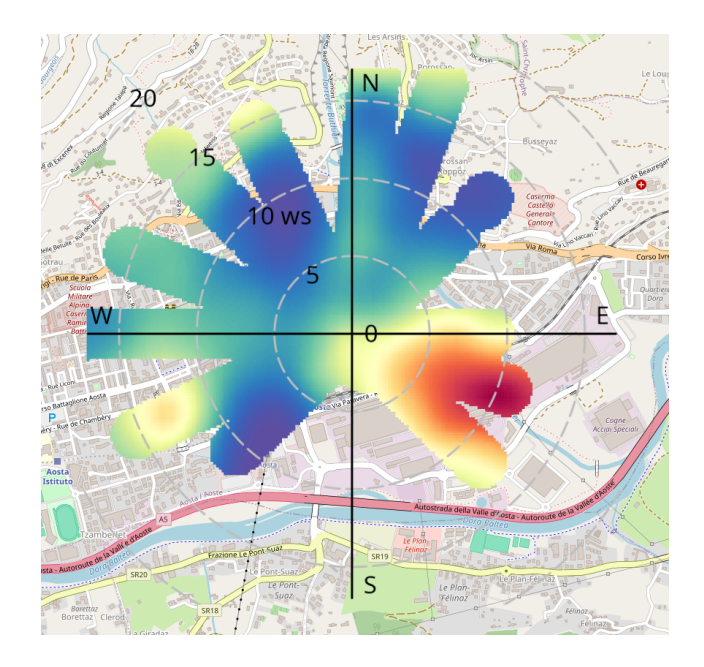


Figure S31: Annual CPF plot for coarse particles and the city map. The highest probability of concentrations exceeding the $75^{\rm th}$ percentile is associated to southesterly winds.

337 S15 Case study: traffic exhaust and non-exhaust during winter holidays 338 days 2024

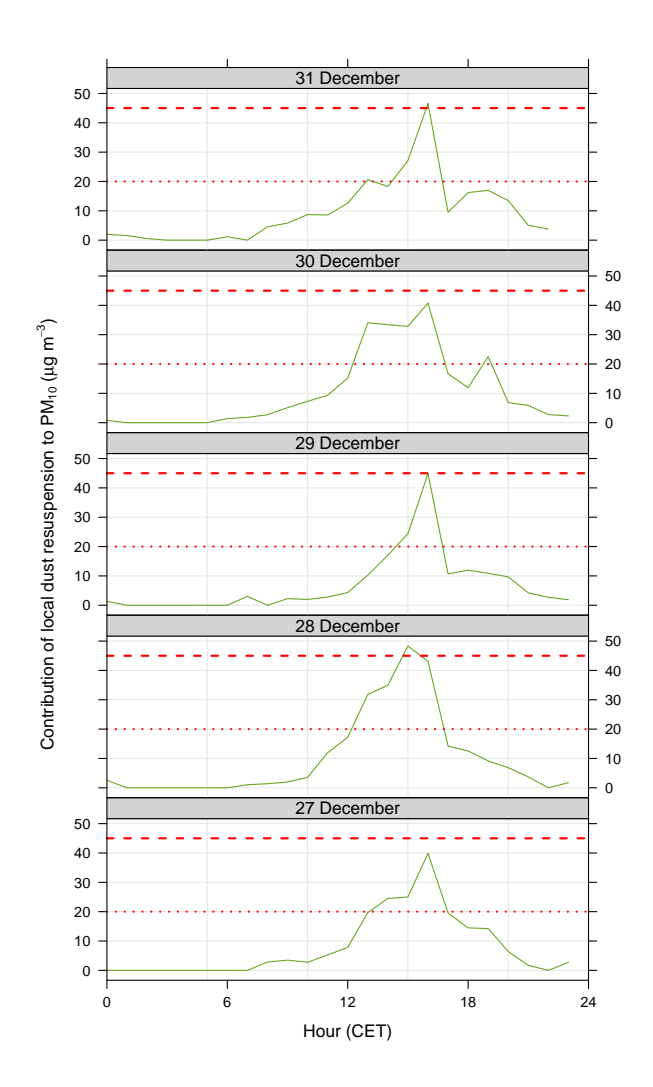


Figure S32: Contribution of local dust resuspension to PM_{10} in Aosta–Downtown, as determined from RASPBERRY, in the period 27–31 December 2024. Red horizontal lines: PM_{10} annual and daily average limit values introduced by the 2024/2881/EC AQ directive.

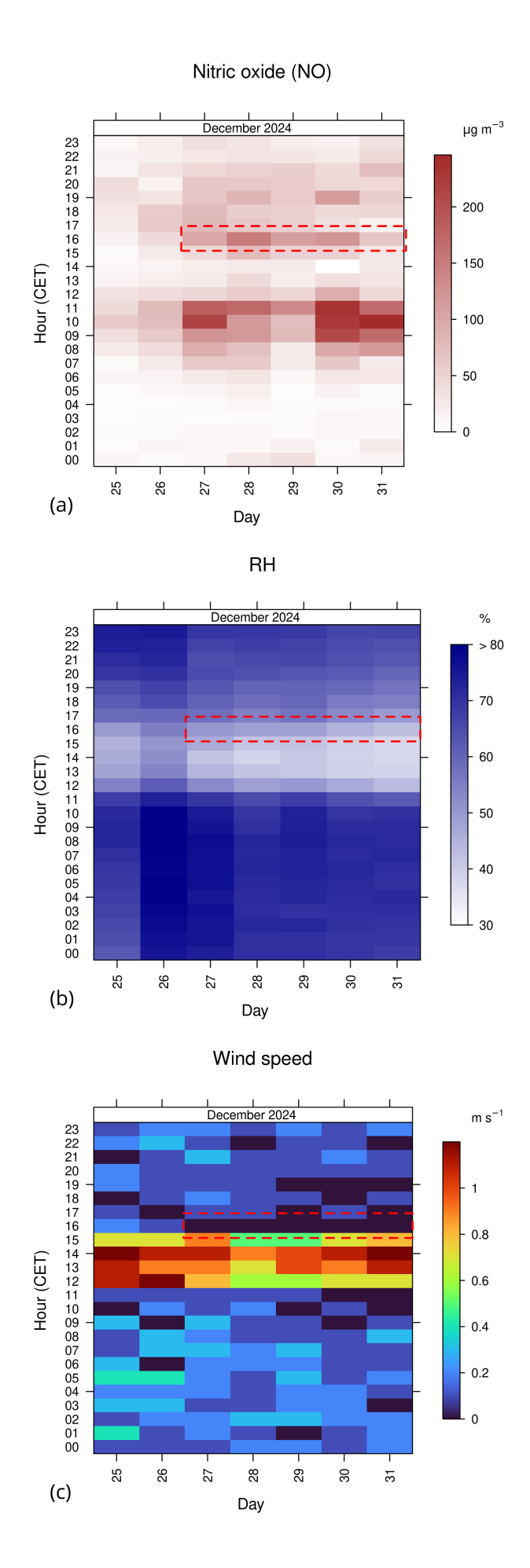


Figure S33: Day/hour diagrams depicting (a) nitric oxide concentrations, (b) relative humidity, and (c) wind speed from 25 to 31 December 2024. The period of peak coarse particle concentrations in the afternoon is highlighted with a dashed contour.

S16 Case study: summertime advection of secondary particles

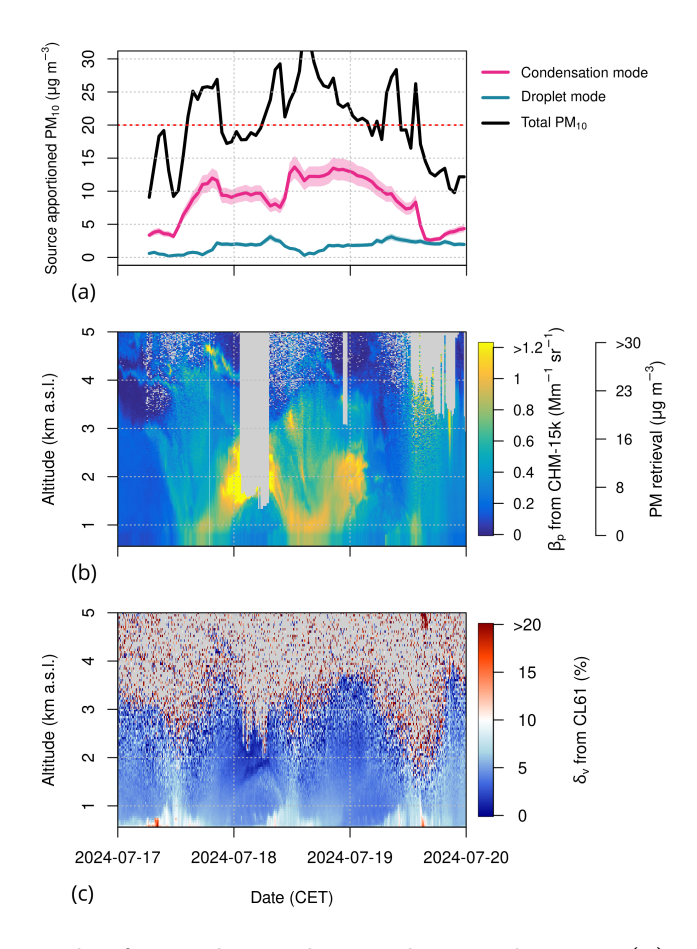


Figure S34: Transport episode of secondary-rich particles in July 2024. (a) PM_{10} contributions from the condensation and droplet mode factors, derived through the physical source apportionment. Red horizontal line: PM_{10} (annual average) limit value introduced by the 2024/2881/EC AQ directive plotted as reference. (b) Vertical profile of ALICENET PM retrievals based on CHM-15k ALC particle backscatter measurements, showing the arrival of an aerosol-rich air mass on the afternoon of 17 July 2024, the formation of a residual layer overnight, and its subsequent entrainment, likely reinforced by additional advection, over the course of the following day. (c) Volume depolarisation ratio from the CL61 ALC.

340 S17 Case study: smoke transport from Canada in 2024

During the event, analysed here from 20 to 24 August 2024, the AOD at 500 nm measured by the sun photometer increases to 0.3–0.4. Larger AOD values are observed in the morning, with sharp decreases during the day, possibly indicating the presence of hygroscopic material. The extinction Ångström exponent remains about 1.3–1.5 throughout the event. The single scattering albedo consistently stays at 0.9 and above. The size distribution shows a maximum between 0.2 and 0.3 µm radius.

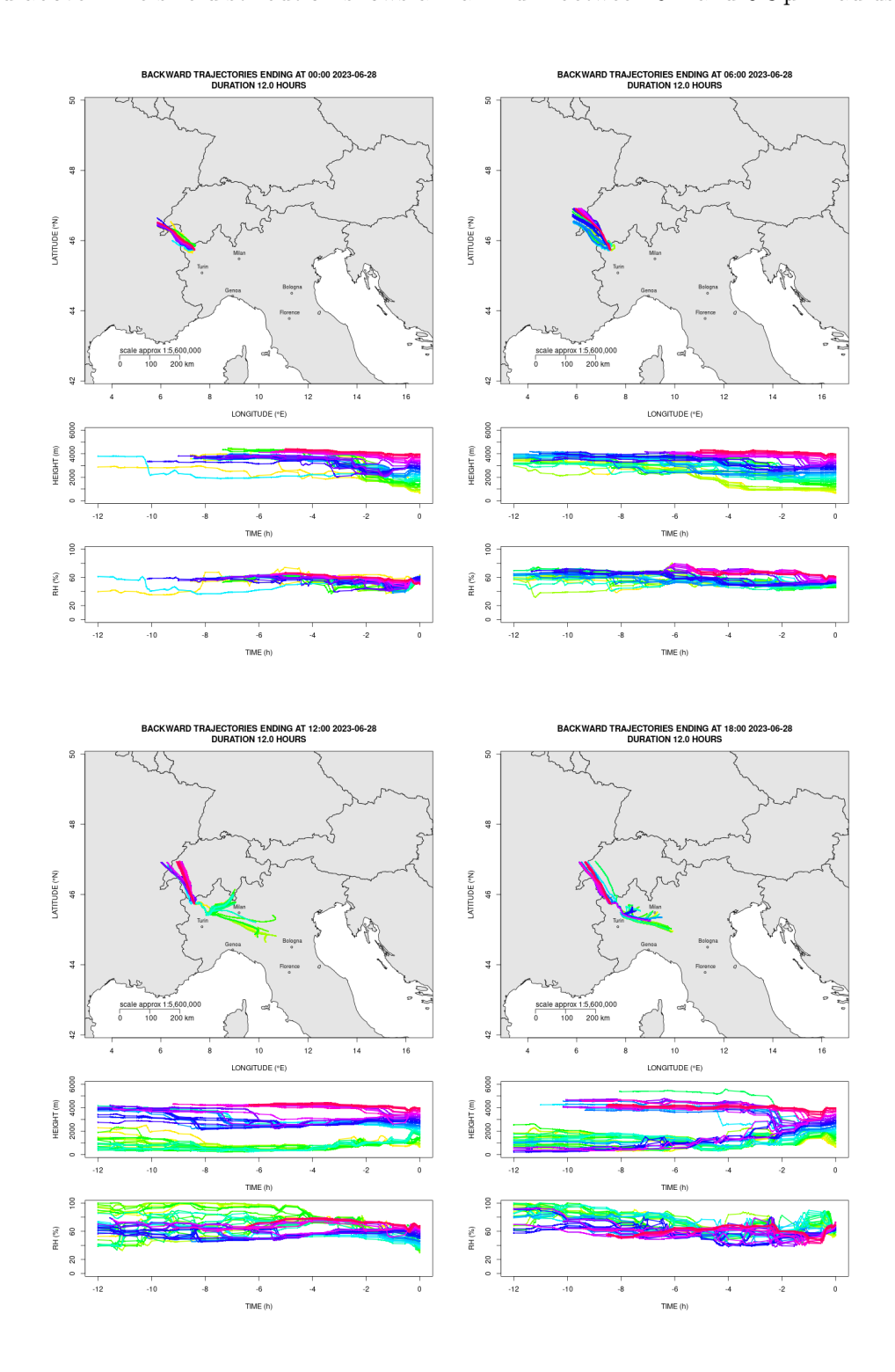


Figure S35: Back-trajectories obtained using the Consortium for Small-scale Modelling (COSMO) model on 28 June 2023, at 6-hour intervals from midnight (see Diémoz et al. (2019) for details of the calculations). The altitude of the back-trajectories and the relative humidity of the corresponding air masses are also displayed. The trajectories are truncated northwest of the Aosta Valley due to the domain boundary of the Italian COSMO model variant.

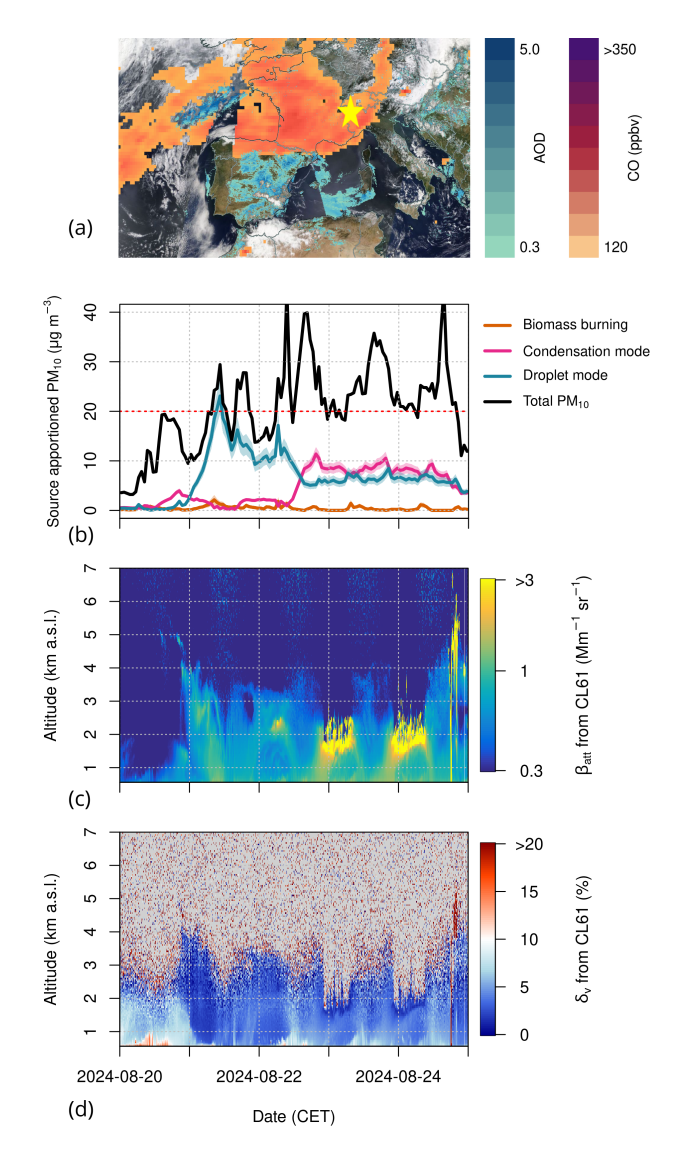


Figure S36: Transport of smoke from Canada to Europe in August 2024. (a) Satellite image (21 August 2024) with a MODIS/Terra corrected reflectance background. Aosta is indicated by a star marker. Aerosol Optical Depth (AOD) at 470 nm, retrieved from the MODIS spectroradiometer onboard the Terra and Aqua satellites (MAIAC algorithm, product MCD19A2, 1-km resolution), and carbon monoxide concentrations at 500 hPa from nighttime AIRS/Aqua measurements (v7 NRT, L2) are superimposed using two different colour scales (source: worldview.earthdata.nasa.gov). (b) PM₁₀ contributions from the condensation and droplet modes, derived from RASPBERRY. Red horizontal line: PM₁₀ (annual average) limit value introduced by the 2024/2881/EC AQ directive plotted as reference. (c) Vertical profiles of attenuated backscatter from the CL61 ALC. Notice the logarithmic colour scale. The CHM-15k ALC was temporarily installed at another station and ALICENET PM inversions from CL61 are not yet supported. (d) Volume depolarisation ratio from the CL61 ALC.

346 S18 Seasonal splitting

As part of this study, we investigated whether seasonal PMFs could improve RASPBERRY source identification. The profiles obtained separately for each season (not shown) differ significantly from the annual PMF, particularly for winter and summer. For instance, while the winter PMF identifies the same profiles as the annual PMF, it fails to correctly assign PM₁₀ mass contributions to each factor. Specifically, the traffic emissions and secondary droplet mode factors are approximately half of those obtained with the annual PMF, whereas the secondary condensation and dust factors are 25–30 % higher. These discrepancies contradict the results from the chemical PMF. We attribute this behavior to the overlap of several sources during winter, the persistence of their emitted particles in the atmosphere, and the modulation of their concentrations by meteorological conditions. Indeed, at the particular

study site, meteorology is a main driver of PM₁₀ concentrations and a confounding factor. For example, 356 strong temperature inversions can increase pollutant concentrations at the surface, while Foehn winds 357 can dramatically decrease them, introducing strong correlations between species. This large rotational 358 ambiguity is particularly evident in the G-space PMF plots, where clear edges are visible especially for 359 fine modes and cannot be mitigated by F-peak rotations. Conversely, in the summer PMF, certain 360 factors such as the droplet mode and biomass burning are almost absent. In place of the latter, for 361 instance, a factor emerges with a large Delta-C and a flat VSD, which deviates significantly from the 362 annual biomass burning profile. As a consequence, contributions differ as well: traffic emissions are 363 50 % higher compared to the annual PMF for the same season, residential biomass burning is 150 %364 higher, and the separation between desert dust and local coarse particles is poorer. As a confirmation 365 of our hypothesis, the spring and autumn PMFs are more consistent with the annual results. Indeed, 366 during these transitional seasons, various emission sources alternate, enabling better factor separation. 367

368 References

- Allen, G. A., Miller, P. J., Rector, L. J., Brauer, M., and Su, J. G.: Characterization of Valley Winter Woodsmoke Concentrations in Northern NY Using Highly Time-Resolved Measurements, Aerosol and Air Qual. Res., 11, 519–530, https://doi.org/10.4209/aaqr.2011.03.0031, 2011.
- Ashbaugh, L. L., Malm, W. C., and Sadeh, W. Z.: A residence time probability analysis of sulfur concentrations at grand Canyon National Park, Atmos. Environ., 19, 1263–1270, https://doi.org/10.1016/0004-6981(85)90256-2, 1985.
- Aujay-Plouzeau, R.: Guide méthodologique pour la mesure du «Black Carbon» par Aethalomètre multi longueur d'onde AE33 dans l'air ambiant (Version 2020), Tech. rep., Ineris, https://www.lcsqa.org/system/files/media/documents/LCSQA2019-Guide_mesure_ BlackCarbon_par_AE33_VF03-Approuv%C3%A9CPS15122020.pdf, 2020.
- Barreto, A., Cuevas, E., García, R. D., Carrillo, J., Prospero, J. M., Ilić, L., Basart, S., Berjón, A. J.,
 Marrero, C. L., Hernández, Y., Bustos, J. J., Ničković, S., and Yela, M.: Long-term characterisation
 of the vertical structure of the Saharan Air Layer over the Canary Islands using lidar and radiosonde
 profiles: implications for radiative and cloud processes over the subtropical Atlantic Ocean, Atmos.
 Chem. Phys., 22, 739–763, https://doi.org/10.5194/acp-22-739-2022, 2022.
- Bellini, A., Diémoz, H., Di Liberto, L., Gobbi, G. P., Bracci, A., Pasqualini, F., and Barnaba, F.: ALICENET – an Italian network of automated lidar ceilometers for four-dimensional aerosol monitoring: infrastructure, data processing, and applications, Atmos. Meas. Tech., 17, 6119–6144, https://doi.org/10.5194/amt-17-6119-2024, 2024.
- Bernardoni, V., Pileci, R. E., Caponi, L., and Massabò, D.: The Multi-Wavelength Absorption
 Analyzer (MWAA) Model as a Tool for Source and Component Apportionment Based on Aerosol
 Absorption Properties: Application to Samples Collected in Different Environments, Atmosphere, 8,
 https://doi.org/10.3390/atmos8110218, 2017.
- Bhandari, S., Arub, Z., Habib, G., Apte, J. S., and Hildebrandt Ruiz, L.: Source apportionment resolved by time of day for improved deconvolution of primary source contributions to air pollution, Atmos. Meas. Tech., 15, 6051–6074, https://doi.org/10.5194/amt-15-6051-2022, 2022.
- Chien, C.-H., Theodore, A., Wu, C.-Y., Hsu, Y.-M., and Birky, B.: Upon correlating diameters measured by optical particle counters and aerodynamic particle sizers, J. Aerosol Sci., 101, 77–85, https://doi.org/10.1016/j.jaerosci.2016.05.011, 2016.
- Diémoz, H., Gobbi, G. P., Magri, T., Pession, G., Pittavino, S., Tombolato, I. K. F., Campanelli,
 M., and Barnaba, F.: Transport of Po Valley aerosol pollution to the northwestern Alps Part
 Long-term impact on air quality, Atmos. Chem. Phys., 19, 10129–10160, https://doi.org/10.5194/acp-19-10129-2019, 2019.

- Diémoz, H., Tombolato, I. K. F., Zublena, M., Magri, T., and Ferrero, L.: The impact of biomass burning
 emissions on PM concentration in the Greater Alpine region, in: Proceedings of 12th International
 Conference on Air Quality, Science and Application, p. 26, Hatfield, UK, 10.18745/pb.22217, 2020.
- European Commission: Directive 2008/50/EC of the European Parliament and of the Council on ambient air quality and cleaner air for Europe, in: 2008/50/EC, edited by European Parliament, 2008.
- Ferrero, L., Mocnik, G., Ferrini, B., Perrone, M., Sangiorgi, G., and Bolzacchini, E.: Vertical profiles of aerosol absorption coefficient from micro-Aethalometer data and Mie calculation over Milan, Sci.

 Total Environ., 409, 2824–2837, https://doi.org/10.1016/j.scitotenv.2011.04.022, 2011.
- Ferrero, L., Losi, N., Rigler, M., Gregorič, A., Colombi, C., D'Angelo, L., Cuccia, E., Cefalì, A., Gini,
 I., Doldi, A., Cerri, S., Maroni, P., Cipriano, D., Markuszewski, P., and Bolzacchini, E.: Determining
 the Aethalometer multiple scattering enhancement factor C from the filter loading parameter, Sci.
 Total Environ., 917, 170 221, https://doi.org/10.1016/j.scitotenv.2024.170221, 2024.
- Forello, A. C., Bernardoni, V., Calzolai, G., Lucarelli, F., Massabò, D., Nava, S., Pileci, R. E., Prati, P.,
 Valentini, S., Valli, G., and Vecchi, R.: Exploiting multi-wavelength aerosol absorption coefficients in a
 multi-time resolution source apportionment study to retrieve source-dependent absorption parameters,
 Atmos. Chem. Phys., 19, 11 235–11 252, https://doi.org/10.5194/acp-19-11235-2019, 2019.
- Forello, A. C., Cunha-Lopes, I., Almeida, S. M., Alves, C. A., Tchepel, O., Crova, F., and Vecchi, R.: Insights on the combination of off-line and on-line measurement approaches for source apportionment studies, Sci. Total Environ., 900, 165 860, https://doi.org/10.1016/j.scitotenv.2023.165860, 2023.
- Grange, S. K., Lötscher, H., Fischer, A., Emmenegger, L., and Hueglin, C.: Evaluation of equivalent black carbon source apportionment using observations from Switzerland between 2008 and 2018, Atmos. Meas. Tech., 13, 1867–1885, https://doi.org/10.5194/amt-13-1867-2020, 2020.
- Gu, J., Pitz, M., Schnelle-Kreis, J., Diemer, J., Reller, A., Zimmermann, R., Soentgen, J., Stoelzel, M.,
 Wichmann, H.-E., Peters, A., and Cyrys, J.: Source apportionment of ambient particles: Comparison of positive matrix factorization analysis applied to particle size distribution and chemical composition data, Atmos. Environ., 45, 1849–1857, https://doi.org/10.1016/j.atmosenv.2011.01.009, 2011.
- Hasheminassab, S., Pakbin, P., Delfino, R. J., Schauer, J. J., and Sioutas, C.: Diurnal and seasonal
 trends in the apparent density of ambient fine and coarse particles in Los Angeles, Environ. Pollut.,
 187, 1–9, https://doi.org/10.1016/j.envpol.2013.12.015, 2014.
- Hayfield, T. and Racine, J. S.: Nonparametric Econometrics: The np Package, J. Stat. Softw., 27, 1–32, https://doi.org/10.18637/jss.v027.i05, 2008.
- Marsteen, L. and Hak, C.: NILU Report 21/2021: PM10/PM2.5 comparison exercise in Oslo, Norway.
 Study in 2015–2016 and 2018, Tech. rep., Norwegian Institute for Air Research (NILU), ISBN 978-82-425-3059-2, ISSN 2464-3327, 2021.
- Norris, G., Duvall, R., and Brown, S.: EPA Positive Matrix Factorization (PMF) 5.0 Fundamentals and User Guide, U.S. Environmental Protection Agency Office of Research and Development Washington, DC 20460, https://www.epa.gov/sites/default/files/2015-02/documents/pmf_5.

 O_user_guide.pdf, ePA/600/R-14/108, 2014.
- Ogulei, D., Hopke, P. K., Zhou, L., Pancras, J. P., Nair, N., and Ondov, J. M.: Source apportionment of
 Baltimore aerosol from combined size distribution and chemical composition data, Atmos. Environ.,
 40, 396–410, https://doi.org/10.1016/j.atmosenv.2005.11.075, 2006.
- Ogulei, D., Hopke, P. K., Chalupa, D. C., , and Utell, M. J.: Modeling Source Contributions to Submicron Particle Number Concentrations Measured in Rochester, New York, Aerosol Sci. Tech., 41, 179–201, https://doi.org/10.1080/02786820601116012, 2007.
- Paatero, P.: Interactive comment on Atmos. Chem. Phys. Discuss., 10.5194/acp-2018-784, https://acp.copernicus.org/preprints/acp-2018-784/acp-2018-784-RC2.pdf, 2018.

- Pakkanen, T. A., Kerminen, V.-M., Korhonen, C. H., Hillamo, R., Aarnio, P., Koskentalo, T., and
 Maenhaut, W.: Use of atmospheric elemental size distributions in estimating aerosol sources in
 the Helsinki area, Atmos. Environ., 35, 5537–5551, https://doi.org/10.1016/S1352-2310(01)00232-1,
 2001.
- PALAS GmbH: Report on supplementary testing of the Fidas® 200 S respectively Fidas® 200 measuring system manufactured by PALAS GmbH for the components suspended particulate matter PM10 and PM2.5, TÜV-report: 936/21227195/C, chap. Operating Manual Fine Dust Monitor System Fidas® Version V0230816, TÜV Rheinland Energie und Umwelt GmbH, https://www.palas.de/file/ea8697/application/octet-stream/Palas+T%C3%9CV+Fidas+System, 2016.
- Patton, A., Politis, D. N., and White, H.: Correction to "Automatic Block-Length Selection for the Dependent Bootstrap" by D. Politis and H. White, Economet. Rev., 28, 372–375, https://doi.org/10.1080/07474930802459016, 2009.
- Pletscher, K., Weiß, M., and Mölter, L.: Simultaneous determination of PM fractions, particle number and particle size distribution in high time resolution applying one and the same optical measurement technique, Gefahrst. Reinhalt. L., 76, 425–436, 2016.
- Regione Valle d'Aosta: Aerial photograph of Aosta from GeoBrowser, https://mappe.regione.vda. it/pub/geoCartoSCT/, 2021.
- Rigler, M., Drinovec, L., Lavrič, G., Vlachou, A., Prévôt, A. S. H., Jaffrezo, J. L., Stavroulas, I., Sciare,
 J., Burger, J., Kranjc, I., Turšič, J., Hansen, A. D. A., and Močnik, G.: The new instrument using a
 TC-BC (total carbon-black carbon) method for the online measurement of carbonaceous aerosols,
 Atmos. Meas. Tech., 13, 4333-4351, https://doi.org/10.5194/amt-13-4333-2020, 2020.
- Rivas, I., Beddows, D. C., Amato, F., Green, D. C., Järvi, L., Hueglin, C., Reche, C., Timonen, H., Fuller, G. W., Niemi, J. V., Pérez, N., Aurela, M., Hopke, P. K., Alastuey, A., Kulmala, M., Harrison, R. M., Querol, X., and Kelly, F. J.: Source apportionment of particle number size distribution in urban background and traffic stations in four European cities, Environ. Int., 135, 105 345, https://doi.org/10.1016/j.envint.2019.105345, 2020.
- Rolph, G., Stein, A., and Stunder, B.: Real-time Environmental Applications and Display sYstem: READY, Environ. Modell. Softw., 95, 210–228, https://doi.org/10.1016/j.envsoft.2017.06.025, 2017.
- Romonosky, D. E., Ali, N. N., Saiduddin, M. N., Wu, M., Lee, H. J. J., Aiona, P. K., and Nizkorodov, S. A.: Effective absorption cross sections and photolysis rates of anthropogenic and biogenic secondary organic aerosols, Atmos. Environ., 130, 172–179, https://doi.org/10.1016/j.atmosenv.2015.10.019, 2016.
- Salma, I., Ocskay, R., Raes, N., and Maenhaut, W.: Fine structure of mass size distributions in an urban environment, Atmos. Environ., 39, 5363–5374, https://doi.org/10.1016/j.atmosenv.2005.05.021, 2005.
- Savadkoohi, M., Pandolfi, M., Favez, O., Putaud, J.-P., Eleftheriadis, K., Fiebig, M., Hopke, P. K., 484 Laj, P., Wiedensohler, A., Alados-Arboledas, L., Bastian, S., Chazeau, B., Álvaro Clemente María, 485 Colombi, C., Costabile, F., Green, D. C., Hueglin, C., Liakakou, E., Luoma, K., Listrani, S., 486 Mihalopoulos, N., Marchand, N., Močnik, G., Niemi, J. V., Ondráček, J., Petit, J.-E., Rattigan, O. V., 487 Reche, C., Timonen, H., Titos, G., Tremper, A. H., Vratolis, S., Vodička, P., Funes, E. Y., Zíková, N., 488 Harrison, R. M., Petäjä, T., Alastuey, A., and Querol, X.: Recommendations for reporting equivalent 489 black carbon (eBC) mass concentrations based on long-term pan-European in-situ observations, 490 Environ. Int., 185, 108 553, https://doi.org/10.1016/j.envint.2024.108553, 2024. 491
- Savadkoohi, M., Sofowote, U. M., Querol, X., Alastuey, A., Pandolfi, M., and Hopke, P. K.: Source-dependent absorption Ångström exponent in the Los Angeles Basin: Multi-time resolution factor analyses of ambient PM2.5 and aerosol optical absorption, Sci. Total Environ., 958, 178 095, https://doi.org/10.1016/j.scitotenv.2024.178095, 2025.

- Sowlat, M. H., Hasheminassab, S., and Sioutas, C.: Source apportionment of ambient particle number concentrations in central Los Angeles using positive matrix factorization (PMF), Atmos. Chem. Phys., 16, 4849–4866, https://doi.org/10.5194/acp-16-4849-2016, 2016.
- Stein, A. F., Draxler, R. R., Rolph, G. D., Stunder, B. J. B., Cohen, M. D., and Ngan, F.: NOAA's
 HYSPLIT Atmospheric Transport and Dispersion Modeling System, Bull. Amer. Meteor. Soc., 96,
 2059 2077, https://doi.org/10.1175/BAMS-D-14-00110.1, 2015.
- Thimmaiah, D., Hovorka, J., and Hopke, P. K.: Source apportionment of winter submicron prague aerosols from combined particle number size distribution and gaseous composition data, Aerosol Air Qual. Res., 9, 209–236, https://doi.org/10.4209/aaqr.2008.11.0055, 2009.
- Vecchi, R., Bernardoni, V., Paganelli, C., and Valli, G.: A filter-based light-absorption measurement
 with polar photometer: Effects of sampling artefacts from organic carbon, J. Aerosol Sci., 70, 15–25,
 https://doi.org/10.1016/j.jaerosci.2013.12.012, 2014.
- Vörösmarty, M., Hopke, P. K., and Salma, I.: Attribution of aerosol particle number size distributions
 to main sources using an 11-year urban dataset, Atmos. Chem. Phys., 24, 5695–5712, https://doi.org/
 10.5194/acp-24-5695-2024, 2024.
- Vu, T. V., Delgado-Saborit, J. M., and Harrison, R. M.: Review: Particle number size distributions
 from seven major sources and implications for source apportionment studies, Atmos. Environ., 122,
 114–132, https://doi.org/10.1016/j.atmosenv.2015.09.027, 2015.
- Wang, Y., Hopke, P. K., Rattigan, O. V., Xia, X., Chalupa, D. C., and Utell, M. J.: Characterization
 of Residential Wood Combustion Particles Using the Two-Wavelength Aethalometer, Environ. Sci.
 Tech., 45, 7387–7393, https://doi.org/10.1021/es2013984, 2011.
- Weingartner, E., Saathoff, H., Schnaiter, M., Streit, N., Bitnar, B., and Baltensperger, U.: Absorption of light by soot particles: determination of the absorption coefficient by means of aethalometers, J. Aerosol Sci., 34, 1445–1463, https://doi.org/10.1016/S0021-8502(03)00359-8, 2003.
- Xie, M., Chen, X., Holder, A. L., Hays, M. D., Lewandowski, M., Offenberg, J. H., Kleindienst, T. E.,
 Jaoui, M., and Hannigan, M. P.: Light absorption of organic carbon and its sources at a southeastern
 U.S. location in summer, Environ. Pollut., 244, 38–46, https://doi.org/10.1016/j.envpol.2018.09.125,
 2019.
- Zanatta, M., Gysel, M., Bukowiecki, N., Müller, T., Weingartner, E., Areskoug, H., Fiebig, M.,
 Yttri, K., Mihalopoulos, N., Kouvarakis, G., Beddows, D., Harrison, R., Cavalli, F., Putaud, J.,
 Spindler, G., Wiedensohler, A., Alastuey, A., Pandolfi, M., Sellegri, K., Swietlicki, E., Jaffrezo, J.,
 Baltensperger, U., and Laj, P.: A European aerosol phenomenology-5: Climatology of black carbon
 optical properties at 9 regional background sites across Europe, Atmos. Environ., 145, 346–364,
 https://doi.org/10.1016/j.atmosenv.2016.09.035, 2016.
- Zhou, L., Hopke, P. K., Paatero, P., Ondov, J. M., Pancras, J., Pekney, N. J., and Davidson, C. I.:
 Advanced factor analysis for multiple time resolution aerosol composition data, Atmos. Environ., 38,
 4909–4920, https://doi.org/10.1016/j.atmosenv.2004.05.040, 2004.
- Zhou, L., Hopke, P. K., Stanier, C. O., Pandis, S. N., Ondov, J. M., and Pancras, J. P.: Investigation
 of the relationship between chemical composition and size distribution of airborne particles by
 partial least squares and positive matrix factorization, J. Geophys. Res., 110, https://doi.org/
 10.1029/2004JD005050, 2005a.
- Zhou, L., Kim, E., Hopke, P. K., Stanier, C., and Pandis, S. N.: Mining airborne particulate size distribution data by positive matrix factorization, J. Geophys. Res., 110, https://doi.org/10.1029/2004JD004707, 2005b.
- Zotter, P., Herich, H., Gysel, M., El-Haddad, I., Zhang, Y., Močnik, G., Hüglin, C., Baltensperger, U.,
 Szidat, S., and Prévôt, A. S. H.: Evaluation of the absorption Ångström exponents for traffic and
 wood burning in the Aethalometer-based source apportionment using radiocarbon measurements of
 ambient aerosol, Atmos. Chem. Phys., 17, 4229–4249, https://doi.org/10.5194/acp-17-4229-2017,
 2017.